Quantifying the distribution of nanodiamonds in pre-Younger Dryas to recent age deposits along Bull Creek, Oklahoma Panhandle, USA

Leland C. Bement[a,1], Andrew S. Madden[b], Brian J. Carter[c], Alexander R. Simms[d], Andrew L. Swindle[b], Hanna M. Alexander[d], Scott Fine[c], and Mourad Benamara[e]

[a]Oklahoma Archeological Survey and [b]School of Geology and Geophysics, University of Oklahoma, Norman, OK 73019; [c]Department of Plant and Soil Sciences, Oklahoma State University, Stillwater, OK 74078; [d]Department of Earth Science, University of California, Santa Barbara, CA 93106; and [e]Institute for Nanoscience and Engineering, University of Arkansas, Fayetteville, AR 72701

Edited by Henry J. Melosh, Purdue University, West Lafayette, IN, and approved December 23, 2013 (received for review May 22, 2013)

High levels of nanodiamonds (nds) have been used to support the transformative hypothesis that an extraterrestrial (ET) event (comet explosion) triggered Younger Dryas changes in temperature, flora and fauna assemblages, and human adaptations [Firestone RB, et al. (2007) *Proc Natl Acad Sci USA* 104(41):16016–16021]. We evaluate this hypothesis by establishing the distribution of nds within the Bull Creek drainage of the Beaver River basin in the Oklahoma panhandle. The earlier report of an abundance spike of nds in the Bull Creek I Younger Dryas boundary soil is confirmed, although no pure cubic diamonds were identified. The lack of hexagonal nds suggests Bull Creek I is not near any impact site. Potential hexagonal nds at Bull Creek were found to be more consistent with graphene/graphane. An additional nd spike is found in deposits of late Holocene through the modern age, indicating nds are not unique to the Younger Dryas boundary. Nd distributions do not correlate with depositional environment, pedogenesis, climate perturbations, periods of surface stability, or cultural activity.

North American Southern Plains | megafauna extinction

A recent hypothesis states that an extraterrestrial (ET) collision triggered the Younger Dryas (YD) chronozone ~10,900 ± 100 radiocarbon years before present (RCYBP) and left event-specific markers, including magnetic grains with iridium, magnetic microspherules, charcoal, soot and polycyclic hydrocarbons, carbon spherules, glass-like carbon, nanodiamonds (nds), and fullerenes with ET helium (1). Opponents of this hypothesis point to the need for outside corroboration of the presence of "above-background levels" of certain markers, including nds (2, 3). In addition, event-marker concentrations need to be quantified in deposits of other periods. This approach requires both the testing of stratified samples immediately above and below those containing ET markers, as reported by Firestone and coworkers (1) and Kennett and colleagues (4), and the search for concentrations of ET markers in similar deposits of other periods to eliminate depositional congruence as the mode of concentrating markers into higher-than-background levels.

Reproducibility and interpretations of various ET markers have proven to be extremely controversial (e.g., refs. 5–10). Nds are no exception: their various phases [cubic, n-diamond, hexagonal (hex)], incredibly tiny size, and similarity to other carbon forms has led to seemingly conflicting reports regarding the identity and distribution of nds in and near YD sediments (e.g., refs. 4, 7, and 11–16). The YD signature afforded by the stable carbon isotope record within the Bull Creek (BC) study area of northwestern Oklahoma (17) attracted ET proponents who then discovered a concentration of cubic nds in two adjacent samples at the YD boundary (YDB) BCI sediments, but not in deposits below or above them (4).

Nanodiamond investigations separate from those of the original Firestone group produced mixed results. Daulton and colleagues (12) reported "No evidence of nds in Younger-Dryas sediments," but their investigation was limited to only crushed "microcharcoal aggregates" from the Murray Springs, Arizona, site. Tian and coworkers (14) identified cubic diamonds in a YD-equivalent layer in Belgium. van Hoesel and colleagues (7) identified cubic nds in glassy carbon, but at a stratigraphic layer approximately 200 y after the YD onset. Neither Daulton and colleagues (12) nor van Hoesel and coworkers (7) examined whole-sediment digestions.

Because nds are one of the proposed ET event markers and have already been reported from the study area, we investigated nd distributions in soils and sediments of the BC valley to address the following questions: What is the spatial, temporal, pedologic, and lithostratigraphic distribution of nds in the BC area? What bearing does this distribution have on the ET hypothesis?

The BC area is centrally located in the Great Plains and is ideally suited for additional intensive investigation (*SI Appendix*, Fig. S1.1). Addressing research questions requires sampling several sites in the BC area and testing for nd concentrations in soils and sediments similar to those at BCI. Criteria used in selecting test profiles included, but were not limited to, similar depositional environment, lithostratigraphy, pedogenic characteristics, and global climatic setting at the time of soil formation (in particular, global atmospheric dynamics). Natural agents that concentrate materials on a surface or within soils and sediments include alluvial, colluvial, and aeolian deposition; surface deflation; pedogenesis; and possible anthropogenic factors.

The foundation for this project was provided by the recent results of multiproxy analyses from the BCI site (18, 19) and the projected expansion to additional key sites in this area. Through a combination of particle size distribution, stable carbon

Significance

In 2007, scientists proposed that the start of the Younger Dryas (YD) chronozone (10,900 radiocarbon years ago) and late Pleistocene extinctions resulted from the explosion of a comet in the earth's atmosphere. The ET event, as it is known, is purportedly marked by high levels of various materials, including nanodiamonds. Nanodiamonds had previously been reported from the Bull Creek, Oklahoma, area. We investigate this claim here by quantifying the distribution of nanodiamonds in sediments of different periods within the Bull Creek valley. We found high levels of nanodiamonds in YD boundary deposits, supporting the previous claim. A second spike in nanodiamonds during the late Holocene suggests that the distribution of nanodiamonds is not unique to the YD.

Author contributions: L.C.B., A.S.M., B.J.C., and A.R.S. designed research; L.C.B., A.S.M., B.J.C., A.R.S., A.L.S., H.M.A., and S.F. performed research; L.C.B., A.S.M., B.J.C., A.R.S., A.L.S., H.M.A., S.F., and M.B. analyzed data; and L.C.B., A.S.M., B.J.C., and A.R.S. wrote the paper.

The authors declare no conflict of interest.

This article is a PNAS Direct Submission.

[1]To whom correspondence should be addressed. E-mail: Lbement@ou.edu.

This article contains supporting information online at www.pnas.org/lookup/suppl/doi:10.1073/pnas.1309734111/-/DCSupplemental.

isotopes, pollen, phytolith, and biostratigraphic analyses, the paleoenvironment from roughly 11,000 to 6,000 RCYBP has been reconstructed (*SI Appendix*, Fig. S1.2) (18).To assess the possibility that concentrations of nds might be present in sediments of other ages, sites with characteristics similar to those at BCI but of earlier and later ages were selected. These additional site localities span other YD-like climatic events such as Bond cycles (Holocene rapid climate change events, including the 8.2-ka event) (20, 21), Dansgaard–Oeschger (DO) cycles of Late Pleistocene rapid climate change events (22, 23), and Heinrich events (24). The profile at BCI meets the requirements for later-age deposits and possible correlation to Bond cycles and Heinrich events, including soils with ages at ∼10,400, ∼9,850, ∼8,670, ∼7,660, and ∼6,200 RCYBP.

On the basis of what we know for buried soils at BCI, their paleosurface stability is cumulic and accompanied by reduced sedimentation rates and soil development. If nd concentrations accrue on these surfaces, then samples from each of the soil A horizons with thicknesses and length of development equal to or greater than that displayed in the sample where Kennett and colleagues (4) identified a spike in nd quantities (∼11,000 RCYBP) should contain comparable or greater densities of nds. One of these soils is easily seen along BC and neighboring drainages.

The upper limit of this roughly 100-cm-thick soil consistently dates to ∼10,280 RCYBP and displays the greatest period of continuous pedogenesis in the BC and surrounding drainages (19), with a deposition rate of 0.17 cm/year. If nd densities are linked to pedogenesis, then greater frequencies should be found in the ∼10,280 RCYBP soil than reside in the ∼11,000 RCYBP soil. Later deposition in the valley is aeolian in nature, with small increments of deposition (0.028 cm/y) from ∼9,800 to 6,200 RCYBP. Soils formed in these aeolian deposits along BC represent six times the stability seen in the alluvial deposits. Accrual of nds on the latest aeolian surfaces should be even greater, with deposition rates of only 0.0074 cm/y, representing 23 times the surface stability displayed in alluvial soils. Again, these aeolian soils should contain nd frequencies in excess to those identified in the ∼11,000-y-old soil formed in alluvium if nd frequency is tied to relative surface stability. If nd frequency is tied to depositional environment, then nd frequency should vary according to alluvium, aeolian, and colluvium.

Another possibility is that nd concentrations correlate with changes in atmospheric dynamics during climate shifts. Because the elevated nd counts within the BCI deposits are found in sediments dating to the initial YDB, similar climate reversal events require analysis. The beginning of some of these events corresponds to increases in global wind-blown dust, which increases the mobility of several chemical constituents and the addition of atmospheric components to soil and sediment surfaces. On the basis of an increased abundance in several chemical species found in the U.S.-Greenland Ice Sheet Program (GISP2) Ice Core, Mayewski and colleagues (25) suggested a more dynamic atmosphere during the time of the YD. Could this have resulted in the elevated amounts of nds found in soils of the YD? Several other climatic cycles are thought to have resulted in increased atmospheric dynamics throughout the late Pleistocene and early to mid-Holocene. The fluxes of other atmospheric components also suggest that the Last Glacial Maximum (LGM) and the earliest part of the deglaciation (∼18–15 ka) had similar atmospheric conditions as the YD (25). Do soils from this period also contain elevated amounts of nds? What about other similar soils from other climatic events, such as the 8.2-ka event, which also shows evidence of elevated atmospheric circulation (26), or those represented by DO cycles and Heinrich events, some of which show elevated atmospheric dust concentrations depending on location (e.g., refs. 25–27)? Soils from these periods are present within the BC drainage area. Investigating sediments associated with one or more of these climatic shifts explores the possibility that climatic shifts somehow concentrated nds.

Sample Selection. Bull Creek is characterized today as an intermittent stream, containing a meandering channel bounded by terraces of decreasing elevation and age. The oldest and highest terrace (T-5) contains sediments dating back to the late Pleistocene incision of the BC channel. The basal gravels and sands are consistent with regional incisions defined in other central and southern Plains drainages (28, 29). The BC sequence begins with late Pleistocene channel incision and initial deposition of sands and gravels from a fit, perennial stream. Later deposition belies increasingly underfit stream flow corresponding to increased regional aridity. Alluvial deposition is replaced with aeolian deposition. This general sequence is consistent with regional depositional reconstructions (29, 30).

The chronology for this study was provided by radiometric assay of total carbon from buried soils described at cutbank exposures along the lower reaches of BC, including the BCI exposure (*SI Appendix*, Table S1.1). Soil carbon contains a mixture of recent carbon from bioturbation, carbon introduced into the soil by pedogenesis, and old carbon resident in the deposited sediments. This mixture of carbon sources yields radiocarbon ages that are inexact and occasionally produce age reversals (*SI Appendix*, Table S1.1). However, when combined with regional sedimentologic, pedologic, biologic, and cultural chronologies, these ages can identify important shifts and trends, including the timing of the YD. The shift from alluvial to aeolian deposition at ∼8,670 ± 90 RCYBP (midsoil) in the BCI profile and at 8,200 ± 60 RCYBP (age at burial) at the Leavengood profile corresponds to regional patterns of increased aridity marked by aeolian deposition (28, 29). Radiocarbon ages were also cross-checked with cultural chronologies and biostratigraphy (18, 19; *SI Appendix*, Table S1.1). The presence of an early Paleoindian age cache attributed to the Clovis culture (19) supports the pre-11,000 RCYBP age for the basal sands and gravels found below the lowest BCI T-5 soil. The late Pleistocene age for the lowest T-5 soil is further supported by the latest occurrence of mammoth remains in the BC valley (18). The only large Rancho La Brean species to survive the late Pleistocene extinctions was *Bison antiquus*, which continues to be seen in BC deposits dating up to and including ∼9,000 RCYBP (31). The chronological distribution of taxa within BC is consistent with regional biostratigraphy (32, 33).

In sum, the radiocarbon assay of bulk carbon from buried soil A horizons and associated cultural and faunal materials provide a late Pleistocene/YD chronology that can be tracked along the BC drainage and that is consistent with regional studies (28, 29, 30, 34).

Previous investigations along BC and within the general Beaver River drainage of the Oklahoma panhandle identified an environmental sequence including the LGM, a YD signature comparable to the GISP2 results (*SI Appendix*, Fig. S1.2) (18, 35), and deposits correlating to other defined environmental events. The mapping of terraces (*SI Appendix*, Figs. S1.3 and S1.4) along the lower portion of the BC drainage identified the BC depositional environment at specific temporal settings. Correlating the depositional sequences found in the various terraces with environmental, pedologic, and lithostratigraphic criteria resulted in the selection of 49 samples for nd extraction and characterization.

Samples for this project were selected from the BCI locality that originally yielded cubic diamonds and n-diamonds (4). Kennett and colleagues (4) found a concentration of nds (both n- and cubic forms) centered on the boundary between two soil A horizons interpreted to be the YDB and equivalent to our samples BC20 and BC21. Samples from this profile range from just before ∼11,000 RCYBP (10,870 +/− 132 y for 20 cm of deposition at an estimated rate of 66 y per 10 cm) to today in a series of alluvial and aeolian deposits containing 10 stacked buried soils (*SI Appendix*, Table S1.2). All levels from just below the ∼11,000 level (YDB) to the modern surface were included in this analysis. In addition, select samples from the Hearth locality, located 0.5 km downstream from BCI, were analyzed. A total of six alluvial samples straddle a cultural layer containing a hearth that provided a radiocarbon age on charcoal of ∼2,540 RCYBP.

Table 1. Results and distribution of nanodiamond analysis

Profile and level	Kennett et al. (4), ppb	ND, ppm	Climate change	Anth*	Age, RCYBP	Depth cmbs
BCI						
BC52		190	Late H		0	0–10
BC51		190	Late H	X	<3,000	10–20
BC50		0				20–26
BC49		0				26–36
BC48		0				36–46
BC47		0	Mid H			46–55
BC46		0	Mid H		6,200 ± 90	55–65
BC45		0				65–77
BC44		0			7,660 ± 80	77–87
BC43		0	8,200			87–97
BC42		0				97–104
BC41		0				104–114
BC40		0			8,670 ± 90	114–124
BC39		0				124–134
BC38		0.45				134–144
BC37		0				144–151
BC36		1.9	PBA		9,850 ± 90	151–161
BC35		0.8				161–171
BC34		0.45				171–179
BC33		0				179–189
BC32		0				189–199
BC31		0	YD		10,410 ± 70	199–210
BC30		0	YD		10,400 ± 120	210–220
BC29		0	YD	X		220–230
BC28	5	0	YD		10,750 ± 70	230–238
BC27		0	YD		10,850 ± 210	238–246
BC26		0	YD			246–252
BC25		0.45	YD		10,640 ± 70	252–262
BC24	3	1.9	YD		10,350 ± 210	262–269
BC23		1.9	YD			279–289
BC22		0	YD		10,870 ± 70	289–298
BC21	100	1.9	YDB		11,070 ± 60	298–307
BC20	90	190	YDB			307–312
BC19	1	0				341–351
Hearth						
22		0.45				100–110
21		0				110–120
20		0				120–132
19		0.45	Late H	X	2,540 ± 40	132–142
18		0				142–153
17		0.45				153–164
Leavengood						
18		1.9				285–292
19		1.9	YD		10,330 ± 70	302–310
20		0.45				331–341
21		0	B/A		12,550 ± 70	365–375
22		1.9				387–399
23		0	DO1			399–405
Blue Mound						
22		0				885–895
23		0	LGM			935–945
24		0	LGM		18,000 ± 70	1,000–1,010

*Anth refers to cultural material associated with these levels. B/A, Bolling/Allerod; DO1, Dansgaard-Oeschger 1; H, Holocene; LGM, Latest Glacial Maximum; PBA, PreBoreal/Atlantic; YD, Younger Dryas, YDB, Younger Dryas Boundary.

The hearth is 3 m downstream from the described and sampled profile. The Hearth site samples represent the late Holocene. Also sampled was the Leavengood profile, a T5 remnant 2 km upstream from BCI. At Leavengood, six samples from a continuous column were collected. This locality has two dated soils, one at ~12,550 RCYBP and another at ~10,330 RCYBP (Table 1). These samples provide the DO1, Bolling/Allerod (B/A), and YD intervals. The last locality included in this study is the Blue Mound site, which is located 5 km east and 8 km south of BCI. Blue Mound is a large dune atop a playa that dates to the LGM. Two samples are from ~18,000-y-old playa deposits, and the third is from the basal aeolian deposit.

Results

Initial observation of BC digestion residues identified carbonaceous grains with irregular boundaries and diameters of several hundred nanometers. The lack of expected 2–20-nm grains in our samples prompted us to apply a sample preparation strategy that maximized the possibility for capturing these types of grains. Digestion residues were centrifuged at 1,111 × *g* for 30 min, with the transmission electron microscope (TEM) grid placed in the bottom of the tube (*SI Appendix*, section 2.3). This technique yielded carbonaceous grains in the 2–20-nm size. Examination of the crystalline nanoparticles by high-angle annular dark-field imaging (Fig. 1*A*), high-resolution transmission electron microscopy (HRTEM) (Fig. 1*B*), electron diffraction (Fig. 1*C*), and energy dispersive X-ray analysis demonstrated that the particles were consistent with n-diamonds. Fast Fourier transforms of the lattice fringes from HRTEM images (e.g., *SI Appendix*, Fig. S3.7) exhibited spacings of 2.02–2.08 Å, 1.78–1.85 Å, and 1.03 Å, consistent with n-diamond (e.g., *SI Appendix*, Table S3.1) (36). X-ray analysis detected only carbon with minor amounts of oxygen from regions of the sample containing the smaller particles sitting on the support film, but hydrogen cannot be detected with this method.

After initial identification of n-diamonds, fresh TEM grids were prepared for all samples with the high-speed centrifugation method. Similar n-diamond particles were subsequently found in several other samples, typically with similar overall morphologies. Nanodiamond internal textures were observed with HRTEM. Lattice fringes often cross entire grains, providing evidence that these crystals are not mixtures of disordered graphite, graphene, and graphane, as observed in other natural and anthropogenic nanoscale carbons (e.g., refs. 37–42). A number of other internal textures were observed. These include "star" twins (Fig. 2*A*), thickness/strain fringes, linear twins (Fig. 2*B*), and nonlinear twins. Such twinning has previously been described specifically for diamond (e.g., refs. 43 and 44), including with HRTEM (e.g., ref. 45). In particular, star twins are a unique morphology with a nearly fivefold symmetry. Fivefold rotation symmetry is rare in crystalline materials, as it cannot alone be used to fill space. Star twins have previously been described for diamond (e.g., refs. 14, 46, and 47). Although they can occur in other nanoparticulate materials such as metals (e.g., ref. 48), observation of these twins in multiple samples with carbonaceous grains supports the identification of diamond. Daulton and colleagues (49) observed similar linear and star twins in detonation nd, chemical vapor deposition (CVD) diamond, and meteoritic diamond. The relative abundance of textures was found to be similar for meteoric and CVD diamonds, suggesting that an analogous process to CVD was responsible for the growth of meteoric diamonds. Because of the relatively small proportion of grains observed with HRTEM in each of our samples, no such interpretation could be made.

Nanodiamond grain sizes are mostly limited to <15 nm (*SI Appendix*, Table S2.2). This is consistent with research demonstrating that H-stabilized nd is thermodynamically preferred over graphite in at least part of this size range (50). Peng and colleagues (51) observed a distinct size difference in nds experimentally produced by high-energy carbon implantation in quartz; 5–7-nm diamonds formed at low doses of carbon were cubic, whereas 8–13-nm grains formed at higher doses were n-diamond. Perhaps the incorporation of hydrogen accommodates additional strain, increasing the stability field of nd. Indeed, the phase transition of graphite to nd occurs at lower (pressure/temperature) conditions for nanoscale particles (52). The large grains initially found

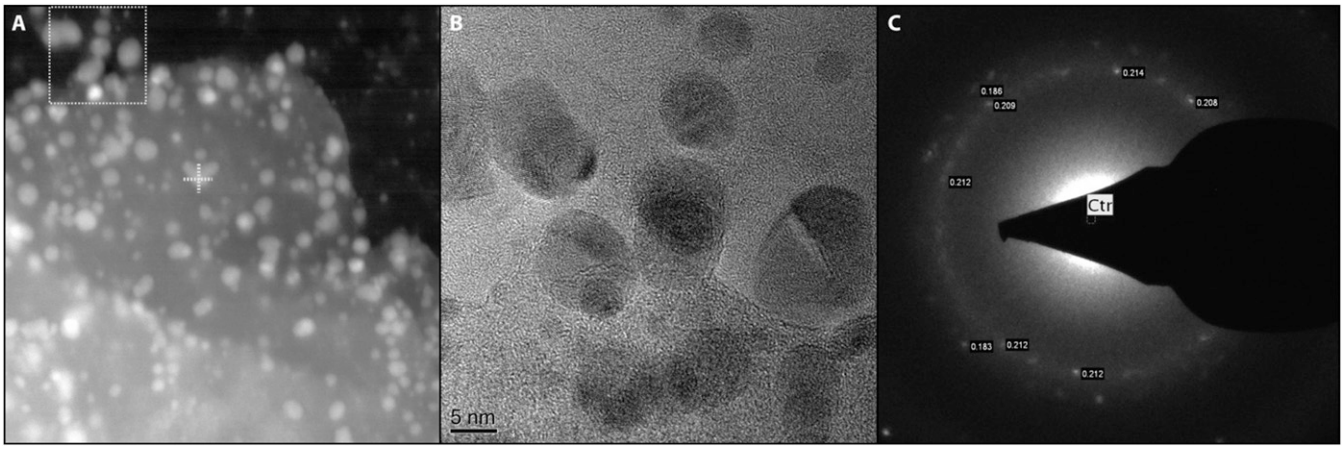

Fig. 1. (*A*) High-angle annular dark-field imaging, (*B*) lattice fringe HRTEM, and (*C*) SAED images collected from an area on the edge of the large single particle in *A*. The area in *B* corresponds to the dashed box in *A*. The cross in *A* corresponds to the point of EELS analysis presented in the *SI Appendix*, Fig. S3.6.

in our study generally appeared analogous to hex nds identified at other sites (11; *SI Appendix*, Fig. S3.1). These grains were almost always aggregates of many subgrains, as evidenced by ring patterns in electron diffraction; however, electron diffraction and electron energy loss spectroscopy (EELS) analyses (*SI Appendix*, Fig. S3.2) demonstrated that these grains were graphene/graphane, as previously suggested by Daulton and colleagues (12). No hex nds were found in BC deposits.

Discussion

Implications of Diamond Investigations for the Impact Hypothesis. Our investigation of BC sediments identified nds primarily as the n-diamond structural form. Bull Creek grains similar to hex diamond (11) were more consistent with graphene/graphane. Diamonds can form in extraterrestrial environments and are present in certain types of meteorites and impact-associated rocks. Two points should be clarified to understand the implications of these observations. First, the n-diamond structure can be considered the same as the cubic structure, but with partial carbon occupancy, hydrogen substitutions, and/or defects that allow the electron diffraction position {200} reflections to appear. Indeed, n-diamonds can form in the laboratory under very similar conditions to those under which cubic diamonds form, including through CVD processes (53, 54). CVD diamond growth has also been identified directly for diamonds associated with meteorites and presolar grains (49). As a consequence, n-diamonds and cubic diamonds can form in terrestrial and extraterrestrial processes. Both n-diamonds and cubic nds were previously identified at BCI (4).

In contrast, the hex diamond structure is significantly different and has been found in nature only in rocks or meteorites that experienced very specific pressure and temperature conditions resulting from shock-conversion of graphite (e.g., ref. 55). Thus, hex diamonds are most likely to be found associated with impact sites (e.g., craters) and not necessarily distributed widely. In fact, a majority of diamonds associated with impacts are of cubic, not hex, form (e.g., refs. 55–58). For example, perhaps the most well-known impact at the Cretaceous–Tertiary boundary formed a well-studied sedimentological layer. Cubic nds were found in multiple investigations of acid-resistant residues of this K–T boundary layer sediment (e.g., refs. 56 and 58). Carbon and nitrogen isotopic signatures of K-T nds indicated they were likely produced on Earth through the impact itself or through interactions of the resulting fireball with the atmosphere (e.g., ref. 59). Similar conclusions were determined for the isotope ratios of nds in YD-equivalent sediments (14). No n-diamonds were reported from the K–T boundary layer, but knowledge of n-diamond at that time was limited, and the authors may have considered any diamonds exhibiting the forbidden reflection as merely a defect version of cubic diamond. Indeed, some authors report that impact diamonds include "highly defective" cubic structures (e.g., ref. 60). Thus, although the presence of hex diamonds is a strong positive indicator of an impact event, the lack of hex diamonds, as in the BCI case, cannot be used to negate the possibility of an impact; instead, it suggests that the point of impact is not nearby.

Nanodiamond Distribution in Space and Time. The search for nds in 49 samples ranging in age from the LGM (ca. 20,000 y ago) to modern times also included samples representing YD-like environmental perturbations, sediments of alluvial and aeolian process, differing periods of surface stability, differing pedologic horizonations, and possible associations with anthropogenic activity. The distribution of samples can be categorized thus: two (4.1%) represent the LGM, one (2%) represents the DO1, one (2%) represents the B/A, two (4.1%) represent the YDB, 11 (22.4%) represent the YD, one (2%) represents the PBA, one (2%) represents the 8.2-ka event, two (4.1%) represent the mid-Holocene, and three (6.1%) represent the late-Holocene periods of climate reversals and periods of increased atmospheric particles (Table 1). The remaining samples (n = 25; 51%) are distributed throughout periods of climatic stability.

Thirty-three (67.3%) of the 49 samples are from alluvial depositions, whereas 16 (32.7%) are aeolian. A total of 37 samples (75.5%) are soil A horizons, 11 (22.4%) are soil B horizons, and 1 (2.0%) is a soil C horizon. Three samples (6.1%) correspond to cultural layers. Nanodiamonds were found in 18 (36.7%) of 49 samples (Table 1). The distribution of confirmed nd occurrences is presented in *SI Appendix*, Figs. S4.1 and 4.2. Nanodiamond quantities range from 1.9 ppm (rank 1), to intermediate level at 1.9–19 ppm (rank 2), and to high concentration of 190 ppm (rank 3;

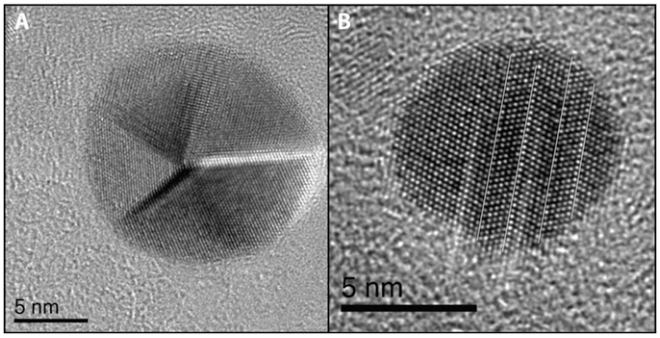

Fig. 2. Nanodiamond textures observed with HRTEM. (*A*) Star twin. (*B*) Multiple linear twins.

SI Appendix, Fig. S4.2). Seven samples fall into rank 1 and eight into rank 2, leaving three of 18 samples (16.7%) in rank 3. It is these three samples that dominate the following discussion.

Eight periods of climatic change accompanied with increased levels of atmospheric particles are represented in the 49 samples of this study. The highest concentrations of nds were only found in two periods, the YDB (n = 1) and Late Holocene (n = 2; Table 1). One of the highest-ranking levels of nd was contained in alluvium, with the remaining two in aeolian deposits, leaving 32 alluvial and 14 aeolian samples without or with low levels of nds. Alluvial samples in the BC1 profile accrued faster than the aeolian samples. If sedimentation rate were a factor concentrating nds, then the slower-accreting aeolian sediments should contain more nds than the alluvial samples. Only three (18.8%) of 16 aeolian samples contained nds compared with 15 (45.5%) of 33 alluvial samples. The low number of both alluvial and aeolian samples with high nd spikes suggests nd accumulation does not correspond to depositional process.

Pedogenesis was not found to be an nd-concentrating factor (*SI Appendix*, Fig. S5.1). Soil A horizons form during periods of relative surface stability in which soil development outperforms sedimentation. Of the three samples with highest levels of nds, two (66.7%) are A horizons; however, these only represent 5.4% (2/37) A horizons. The remaining 94.6% of A horizons did not contain nd spikes.

Nanodiamond concentrations were not correlated with periods of human occupation in the BCI deposits (*SI Appendix*, Fig. S6.1). Distinct cultural zones dated to ∼10,600 RCYBP (level 29), and another at ∼2,000–3,000 RCYBP (level 51), are contained in the deposits. No nd spike accompanies the ∼10,600 RCYBP level. A rank 3 nd spike does, however, occur in the 2,000–3,000-y-old level. Because both cultural layers are replete with hearths and burned lithics and bone, a similar quantity of nds would be expected if this cultural activity were responsible for nd genesis or accumulation.

The nd spike during the 2,000–3,000 RCYBP deposits is enigmatic, first because the nd spike continues beyond the cultural layer to the modern surface, and second because a smaller spike in nd occurrence was identified in the Hearth site deposits of similar age. The Hearth site is a short-term camp dated to 2,540 ± 40 RCYBP. The cultural material included a fire hearth and scatter of tools and bison bone. Sediments from below, at, and above this occupation level were scrutinized for nds. Low quantities (rank 1) of nds were found in three of six samples, but only one sample corresponds to the level of cultural occupation (Table 1). Although this distribution suggests that human activity did not promote the accumulation of nds, the possibility exists that perhaps whatever generated the high nd spike at BCI in a soil A horizon in aeolian deposits is also reflected in the measurable background level of nds in the faster-accruing alluvial deposits at the Hearth site of contemporaneous age to the BCI deposits.

If the YDB and late Holocene concentrations cannot be attributed to specific depositional environments, pedogenesis, periods of environmental perturbations or stability, or cultural activity, then some other n-diamond-producing or concentrating event or condition must have been present at these two times. If an ET source or trigger is to be considered for the YDB spike in nds, then similar consideration would be needed for the late Holocene spike. Searching for such an event is beyond the scope of this article. However, many late Holocene impacts have been documented, including one in Kiowa County, Kansas, ∼160 km northeast of the BC area, that left a 15-m-diameter crater and extensive debris field (53, 61).

Conclusion

The goal of this study was to describe the temporal distribution of nds within the BC drainage of the Beaver River in the Oklahoma panhandle and to evaluate that distribution in light of a proposal that nds are a marker for an extraterrestrial impact that initiated the climatic, biologic, and cultural changes of the YD ∼10,900 RCYBP. Kennett and colleagues (4) had previously identified nds in the BCI profile, including high quantities in samples on either side of the YDB, corresponding to BCI samples 20 and 21 of our study. Our study identified a nd spike of 190 ppm immediately below a soil horizon interpreted as the YDB, diminishing to 1.9 ppm immediately above this soil boundary. Kennett and coworkers found quantities of 1.9 ppb at this soil break that were interpreted by them to be the YDB. Our significantly higher concentration is probably the result of the use of flotation rather than mechanical sieving to obtain the nd-bearing fine-grain samples (*SI Appendix*, section 2.2). We did not, however, conclusively identify the cubic form that had previously been identified by Kennett and colleagues (4). We did identify forms consistent with "highly defective" cubic diamonds. Suspected hex diamonds in the BCI deposits were found to be more consistent with graphene/graphane.

Our findings also identified identical high quantities (190 ppm) of n-diamonds in late-Holocene through present-age deposits at BCI. The second spike of n-diamonds indicates that high levels of nds are not unique to the YDB. The implication of this finding is that either a similar process for concentrating diamonds was acting at both times or a similar event that created the spike at the YDB also occurred during the late Holocene. Similar to Kennett and colleagues (4), we also found low to moderate amounts of nds in samples that could represent background levels. However, most (n = 31 samples; 63%) of the deposits yielded no nds, suggesting there is no reliable background level.

In conclusion, the analysis of 49 sediment samples representing various depositional environments, lithostratigraphic, pedogenic, and global climatic settings identified high levels of nds immediately below and just above YDB deposits and in late-Holocene near-surface deposits. Low quantities (<19 ppm) of nds were found in 15 samples distributed in pre- and post-YDB deposits. Although the high concentration of nds at the YDB along BC may support the ET hypothesis, the high concentration of nds identified in late Holocene deposits indicates such levels are not unique to the YDB.

Methods

Sample collection, preparation, and analysis followed protocols provided by Allen West and published in previous articles (4). Carbonaceous materials were extracted from bulk sediments by digestion and flotation. The resultant concentrate was analyzed by various techniques, including TEM, Select area electron diffraction, energy dispersive spectroscopy, EELS, and HRTEM (*SI Appendix*, sections 2 and 3).

ACKNOWLEDGMENTS. Fieldwork was facilitated by Carolyn Leavengood and John Seaman. This article was greatly enhanced by suggestions from Vance Holliday and an anonymous reviewer. This research was funded in part by National Science Foundation Grant BCS-0918044 (to L.C.B., A.S.M., B.J.C., and A.R.S.). Additional support was received from private donations, especially from Courson Oil and Gas, and the EDMAP program of the US Geological Survey. Institutional support was provided by the University of Oklahoma, Oklahoma State University, and the University of California, Santa Barbara.

1. Firestone RB, et al. (2007) Evidence for an extraterrestrial impact 12,900 years ago that contributed to the megafaunal extinctions and the Younger Dryas cooling. *Proc Natl Acad Sci USA* 104(41):16016–16021.
2. Kerr RA (2008) Paleontology. Experts find no evidence for a mammoth-killer impact. *Science* 319(5868):1331–1332.
3. Pinter N, Ishman SE (2008) Impacts, mega-tsunami, and other extraordinary claims. *GSA Today* 18(1):37–38.
4. Kennett DJ, et al. (2009) Nanodiamonds in the Younger Dryas boundary sediment layer. *Science* 323(5910):94–95.
5. Haynes CV, Jr., et al. (2010) The Murray Springs Clovis site, Pleistocene extinction, and the question of extraterrestrial impact. *Proc Natl Acad Sci USA* 107(9):4010–4015.
6. Pinter N, et al. (2011) The Younger Dryas Impact Hypothesis: A Requiem. *Earth Sci Rev* 106(3-4):247–264.
7. van Hoesel A, et al. (2012) Nanodiamonds and wildfire evidence in the Usselo horizon postdate the Allerod-Younger Dryas boundary. *Proc Natl Acad Sci USA* 109(20):7648–7653.
8. Israde-Alcántara I, et al. (2012) Reply to Blaauw et al., Boslough, Daulton, Gill et al., and Hardiman et al.: Younger Dryas impact proxies in Lake Cuitzeo, Mexico. *Proc Natl Acad Sci USA* 109:E2245–E2247.

9. LeCompte MA, et al. (2012) Independent evaluation of conflicting microspherule results from different investigations of the Younger Dryas impact hypothesis. *Proc Natl Acad Sci USA* 109(44):E2960–E2969.
10. Pigati JS, et al. (2012) Accumulation of impact markers in desert wetlands and implications for the Younger Dryas impact hypothesis. *Proc Natl Acad Sci USA* 109(19): 7208–7212.
11. Kennett DJ, et al. (2009) Shock-synthesized hexagonal diamonds in Younger Dryas boundary sediments. *Proc Natl Acad Sci USA* 106(31):12623–12628.
12. Daulton TL, Pinter N, Scott AC (2010) No evidence of nanodiamonds in Younger-Dryas sediments to support an impact event. *Proc Natl Acad Sci USA* 107(37):16043–16047.
13. Kurbatov AV, et al. (2010) Discovery of a nanodiamond-rich layer in the Greenland ice sheet. *J Glaciol* 56(199):747–757.
14. Tian H, Schryvers D, Claeys P (2011) Nanodiamonds do not provide unique evidence for a Younger Dryas impact. *Proc Natl Acad Sci USA* 108(1):40–44.
15. Daulton TL (2012) Suspect cubic diamond "impact" proxy and a suspect lonsdaleite identification. *Proc Natl Acad Sci USA* 109(34):E2242.
16. Israde-Alcántara I, et al. (2012) Evidence from central Mexico supporting the Younger Dryas extraterrestrial impact hypothesis. *Proc Natl Acad Sci USA* 109(13):E738–E747.
17. Bement LC, Carter BJ (2008) A Younger Dryas Signature on the Southern Plains. *Curr Res Pleist* 25:193–194.
18. Bement LC, Carter BJ, Varney RA, Cummings LS, Sudbury JB (2007) Paleo-Environmental Reconstruction and Bio-Stratigraphy, Oklahoma Panhandle, USA. *Quat Int* 169-170:29–50.
19. Bement L, Schuster K, Carter B (2007) Archeological Survey for Paleo-Indian Sites along the Beaver River, Beaver County, Oklahoma. Oklahoma Archeological Survey Archeological Resource Survey Report No. 54. University of Oklahoma (Oklahoma Archeological Survey, Norman, OK).
20. Bond G, et al. (1997) A Pervasive Millennial-Scale Cycle in North Atlantic Holocene and Glacial Climates. *Science* 278:1257–1266.
21. Bond G, et al. (2001) Persistent solar influence on North Atlantic climate during the Holocene. *Science* 294(5549):2130–2136.
22. Dansgaard W, et al. (1982) A new greenland deep ice core. *Science* 218(4579):1273–1277.
23. Dansgaard W, White JWC, Johnsen SJ (1989) The abrupt termination of the Younger Dryas climate event. *Nature* 339:532–534.
24. Heinrich H (1988) Origin and consequences of cyclic ice rafting in the Northeast Atlantic Ocean during the past 130,000 years. *Quat Res* 29:142–152.
25. Mayewski PA, et al. (1993) Greenland ice core "signal" characteristics offer expanded view of climate change. *J Geophys Res* 98:12,839–12,847.
26. Alley RB, et al. (1997) Holocene Climatic Instability: A Prominent, Widespread Event 8200 Yr Ago. *Geology* 25(6):483–486.
27. Moreno A, et al. (2005) Links between marine and atmospheric processes oscillating on a millennial time-scale. A multi-proxy study of the last 50,000 yr from the Alboran Sea (Western Mediterranean Sea). *Quat Sci Rev* 24:1623–1636.
28. Holliday VT, Meltzer DJ, Mandel R (2011) Stratigraphy of the Younger Dryas Chronozone and Paleoenvironmental Implications: Central and Southern Great Plains. *Quat Int* 242:520–533.
29. Mandel RD (2008) Buried Paleoindian-age Landscapes in Stream Valleys of the Central Plains, USA. *Geomorphology* 101:342–361.
30. Holliday VT (1995) *Stratigraphy and Paleoenvironments of Late Quaternary Valley Fills on the Southern High Plains. Memoir 186* (Geological Society of America, Boulder, Colorado).
31. Bement L, Buehler K, Carter B (2012) Ravenscroft: A Late Paleoindian Bison Kill in the Oklahoma Panhandle. *Oklahoma Anthropol Soc Bull* 60:17–30.
32. Dalquest WW, Baskin JA (1992) Mammals of the Elm Creek Local Fauna, Late Pleistocene of Beaver County, Oklahoma. *Am Midl Nat* 127:13–20.
33. Johnson E (1987) Vertebrate Remains. *Lubbock Lake: Late Quaternary Studies on the Southern High Plains*, ed Johnson E (Texas A&M University Press, College Station), pp 49–89.
34. Haynes CV, Jr. (2008) Younger Dryas "black mats" and the Rancholabrean termination in North America. *Proc Natl Acad Sci USA* 105(18):6520–6525.
35. Bement LC, Carter BJ (2010) Jake Bluff: Clovis Bison Hunting on the Southern Plains of North America. *Am Antiq* 75(4):907–933.
36. Hirai H, Kondo K (1991) Modified phases of diamond formed under shock compression and rapid quenching. *Science* 253(5021):772–774.
37. Bernatowicz TJ, et al. (1996) Constraints on stellar grain formation from presolar graphite in the Murchison meteorite. *Astrophys J* 472:760–782.
38. Fraundorf P, Wackenhut M (2002) The core structure of presolar graphite onions. *Astrophys J* 578:L153–L156.
39. Harris PFJ, Vis RD (2003) High-resolution transmission electron microscopy of carbon and nanocrystals in the Allende meteorite. *Proc R Soc Lond A* 453:2069–2076.
40. Zhu W, Miser DE, Chan WG, Hajaligol MR (2004) HRTEM investigation of some commercially available furnace carbon blacks. *Carbon* 42:1841–1845.
41. Harris PJF (2005) New perspectives on the structures of graphitic carbons. *Crit Rev Solid State Mater Sci* 30:235–253.
42. Croat TK, Stadermann FJ, Bernatowicz TJ (2008) Correlated isotopic and microstructural studies of turbostratic presolar graphites from the Murchison meteorite. *Meteorit Planet Sci* 43(9):1497–1516.
43. Kohn JA (1958) Twinning in diamond-type structures: a proposed boundary-structure model. *Am Mineral* 43:263–284.
44. Shechtman D, Hutchison JL, Robins LH, Farbaugh EN, Feldman A (1993) Growth defects in diamond films. *J Mater Res* 8(3):473–479.
45. van Luyten W, Tendeloo G, Amelinckx S (1992) Electron microscopy study of defects in synthetic diamond layers. *Philos Mag A* 66:899–915.
46. Mani R, Sunkara MK (2003) Kinetic faceting of multiply twinned diamond crystals during vapor phase synthesis. *Diamond & Rel Mat* 12:324–329.
47. Daulton TL (2006) Extraterrestrial nanodiamonds in the cosmos. *Ultrananocrystalline Diamond: Synthesis, Properties, and Applications*, eds Shenderova OA, Gruen DM (William Andrew, Inc., Oxford), pp 23–78.
48. Hofmeister H (2009) Shape variations and anisotropic growth of multiply twinned nanoparticles. *Zeitschriftfür Kristal* 224:528–538.
49. Daulton TL, Eisenhour DD, Bernatowlcz TJ, Lewis RS, Buseck PR (1996) Genesis of presolar diamonds: Comparative high-resolution transmission electronmicroscopy study of meteoritic and terrestrial nano-diamonds. *Geochim Cosmochim Acta* 60:4853–4872.
50. Badzaig P, Verwoerd WS, Ellis WP, Greiner NR (1990) Nanometre-sized diamonds are more stable than graphite. *Nature* 343:244–245.
51. Peng JL, Bursill LA, Jiang B, Orwa JO, Prawer S (2001) Growth of c-diamond, n-diamond and i-carbon nanophases in carbon-ion implanted fused quartz. *Philos Mag B* 81(12):2071–2087.
52. Aleksenskii AE, Baidakova MV, Vul AY, Davydov YV, Pevtsova YA (1997) Diamond-graphite phase transition in ultradisperse-diamond clusters. *Phys Solid State* 39(6): 1007–1015.
53. Wasson JT, Sedwick SP (1969) Possible Sources of Meteoric Material from Hopewell Indian Burial Mounds. *Nature* 222:22–24.
54. Kumar A, et al. (2013) Formation of nanodiamonds at near-ambient conditions via microplasma dissociation of ethanol vapour. *Nat Commun* 4:2618.
55. Hanneman RE, Strong HM, Bundy FP (1967) Hexagonal diamonds in meteorites: implications. *Science* 155(3765):995–997.
56. Carlisle DB, Braman DR (1991) Nanometre-size diamonds in the Cretaceous/Tertiary boundary clay of Alberta. *Nature* 352:708–709.
57. Hough RM, et al. (1995) Diamond and silicon carbide in impact melt rock from the Ries impact crater. *Nature* 378:41–44.
58. Hough RM, Gilmour I, Pillinger CT, Langenhorst F, Montanari A (1997) Diamonds from the iridium-rich K-T boundary layer at Arroyo el Mimbral, Tamaulipas, Mexico. *Geology* 25(11):1019–1022.
59. Gilmour I, et al. (1992) Terrestrial carbon and nitrogen isotopic ratios from cretaceous-tertiary boundary nanodiamonds. *Science* 258(5088):1624–1626.
60. Masaitis VL (1998) Popigai crater: Origin and distribution of diamond-bearing impactites. *Meteorit Planet Sci* 33:349–359.
61. Baillie M (2007) The case for significant numbers of extraterrestrial impacts through the late Holocene. *J Quat Sci* 22:101–109.

SUPPORTING INFORMATION
Quantifying the Distribution of Nanodiamonds in Pre-Younger Dryas to Recent Age Deposits along Bull Creek, Oklahoma Panhandle, USA

Leland C. Bement*[a], Andrew S. Madden[b], Brian J. Carter[c], Alexander R. Simms[d], Andrew L. Swindle[b], Hanna M. Alexander[d], Scott Fine[c], Mourad Benamara[e]

1. Bull Creek site overview

Bull Creek is a right bank tributary to the Beaver River in far western Beaver County, Oklahoma, USA (Figure S1.1).

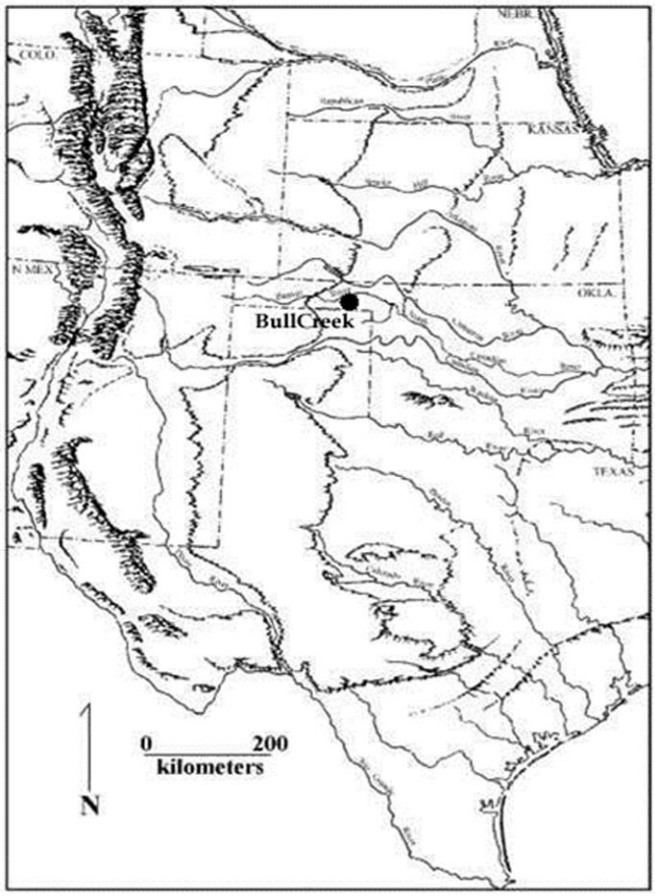

Figure S1.1. The Bull Creek study area, Oklahoma panhandle.

1.1.Bull Creek Chronology

The chronology for this study was provided by radiometric assay of total carbon from buried soils described at cutbank exposures along the lower reaches of Bull Creek, including the BCI exposure (Table S1.1; Table S1.2). With the exception of the initial dating of the BCI exposure where radiocarbon samples were removed from the center of described soils, all other

samples were collected from the upper extent of each soil, thereby providing an age-at-burial. Because the BCI exposure contains a series of stacked cumulic soils, the mid-soil sampling effects little the determination of length of soil formation since the next higher and lower soils provide boundary dates. Additional BCI samples were collected from the top of the lowest four buried soils to provide age-at-burial results for the YDB and subsequent YD soils. In general the sediment ages are stratigraphically consistent, although several dates at BCI appear out of sequence (Table S1.1). These dates are, however, from the same statistical population (3), a symptom of the YD radiocarbon plateau (4). The distinctive YD soils that are easily discernible in all T-5 terrace exposures terminated pedogenesis (were buried) ca 10,280 B.P. with ages at burial of 10,230 $\pm$ 60, 10,280 $\pm$ 60, and 10,280 $\pm$50 RCYBP at the Leavengood, Bull Creek II, and Clovis localities, respectively (Table S1.1). Detailed profile descriptions are provided in Conley (2) and elsewhere (5,6). The detailed BCI profile description is in Table S1.2. The YD soil along Bull Creek fits broader regional patterns (7).

Table S1.1. Radiocarbon assays for the nanodiamond study.

Lab #	Site	Depth (cm)	14C yr B. P.	Cal yr B.P.*	Material**	Source
Beta-249842	Leavengood	70-101	8,200 ± 60	9,166	SOM	(2)
Beta-249843	Leavengood	268-285	10,230 ± 60	11,958	SOM	(2)
Beta-262541	Leavengood	302-331	10,330 ± 70	12,177	SOM	(2)
Beta-249844	Leavengood	365-387	12,550 ± 70	14,740	SOM	(2)
Beta-249845	Leavengood	464-481	13,210 ± 80	16,118	SOM	(2)
Beta-191039	Bull Creek I	50-60	6,200 ± 90	7,094	SOM	(1)
Beta-184850	Bull Creek I	77-87	7,660 ± 80	8,464	SOM	(1)
Beta-191040	Bull Creek I	114-124	8,670 ± 90	9,667	SOM	(1)
Beta-184851	Bull Creek I	151-161	9,850 ± 90	11,286	SOM	(1)
Beta-184852	Bull Creek I	220-229	10,400 ± 120	12,260	SOM	(2)
Beta-262537	Bull Creek I	223-230	10,410 ± 70	12,287	SOM	(2)
Beta-180546	Bull Creek I	234-242	10,850 ± 210	12,765	SOM	(1)***
Beta-262538	Bull Creek I	235-243	10,750 ± 70	12,650	SOM	(2)***
Beta-262539	Bull Creek I	252-260	10,640 ± 70	12,582	SOM	(2)***
Beta-184853	Bull Creek I	262-279	10,350 ± 210	12,118	SOM	(1)***
Beta-262540	Bull Creek I	289-298	10,870 ± 70	12,747	SOM	(2)
Beta-184854	Bull Creek I	289-307	11,070 ± 60	12,962	SOM	(1)
Beta-213704	Hearth	132-142	2,540 ± 40	2,621	Charcoal	(2)
Beta-282304	Blue Mound	935-945	18,000 ± 70	18,000	SOM	This article
Beta-205624	Bull Creek II	180-190	10,280 ± 60	12,059	SOM	(2)
Beta-189108	Clovis	232-235	10,280 ± 50	12,056	SOM	(2)

*Median age calibrated using Calib 6.0 (8)

**SOM, soil organic matter

*** Potential age reversals although results are statistically the same at 95% confidence level (T-test=4.437528, Xi2(.05)=7.81, df= 3; 8)

Table S1.2. Bull Creek I profile description.

Horizon	Depth (cm)	Color Moist	Structure†	Texture‡	Consistence¶	Boundary§	Effervescence††	Special Features
A	0-25	7.5YR4/2	2fGr	SiL	fr	c	ve	loess (unit III); many, fine and m roots.
Ab	46	7.5YR3/2	2fGr	SiL	fr	g	ve	loess (unit III); many, fine and m roots.
Akb2	65	10YR3/3	1fSBK	SiL	fr	c	ve	loess (unit III); many, fine and medium roots; few fine $CaCO_3$ soft bodies in pores.
Akb3	97	10YR3/2	2fSBK	SiL	fr	g	ve	loess (unit III); many, fine and medium roots; common fine $CaCO_3$ soft bodies in pores.
ABkb3	144	10YR3/3	2mSBK	SiL	fr	g	ve	loess (unit III); many fine and medium roots; few fine $CaCO_3$ soft bodies in pores.
2Akb4	171	10YR3/2	2mSBK	SiL	fr	c	ve	colluvium (unit II) few gravels; many fine and medium roots; common fine $CaCO_3$ soft bodies in pores.
2Bkb4	199	7.5YR3/3	2mSBK	L	fr	c	ve	colluvium (unit II); 5% gravels; many fine roots; few fine $CaCO_3$ soft bodies in pores.
2Ab5	231	7.5YR3/2	2mSBK	GCoSL	fr	c	ve	colluvium (unit II); 15% gravels; common fine roots; few fine $CaCO_3$ soft bodies on gravels.
2Ab6	246	7.5YR3/3	1mSBK	SCL	fr	c	ve	colluvium (unit II); 2% gravels; common fine roots; few fine ($CaCO_3$ soft bodies in pores; few very fine charcoal fragments; bison sacral fragment.
2Bwb6	262	7.5YR4/3	1mSBK	CoSL	fr	c	ve	colluvium; few gravels; common fine roots; few fine $CaCO_3$ soft bodies on gravels; bison bone and flakes.
2Akb7	279	7.5YR3/4	2mSBK	SiL	fr	c	ve	colluvium (unit II); few fine roots; common fine $CaCO_3$ soft bodies in pores.
2Bkb7	289	7.5YR4/4	2mSBK	SiL	fr	g	ve	colluvium (unit II); few co. sands; few fine roots; many fine $CaCO_3$ soft bodies in pores.
2Akb8	307	7.5YR4/3	2mSBK	SiL	fr	g	ve	colluvium (unit II); few gravels; few fine roots; many fine $CaCO_3$ soft bodies in pores.
2ACb8	351	7.5YR3/4	1mSBK	L	fr	a	ve	colluvium (unit II); few gravels; few fine roots; few fine $CaCO_3$ soft bodies in pores.
3C1b8	362	7.5YR5/3	SG	VGLCoS	vfr	a	e	alluvium (unit I); 40% gravels; few fine roots; few fine $CaCO_3$ soft bodies on rock fragments.
3C3b8	422	7.5YR4/6	MA	VFSL	fr	a	ve	alluvium (unit I); few fine roots; common fine $CaCO_3$ soft bodies in pores.
3C4b8	473	7.5YR6/4	SG	LS	vfr	a	ve	alluvium (unit I); few gravels; few fine roots.
3C5b8	515	5YR6/4	SG	GCoS	l	a	ve	alluvium (unit I); 30% gravels.
R	615+	2.5YR5/6	MA	-	vfi	-	e	residuum: Permian Cloud Chief sandstone.

Structure†				Texture‡		Consistency¶		Boundary§		Effervescence††	
1	weak	GR	granular	VF	very fine	v	very	c	clear	ve	violent
2	moderate	SBK	subangular blocky	S	sand	fr	friable	g	gradual	e	moderate
f	fine	MA	massive	Si	silt	l	loose	a	abrupt		
m	medium	SG	single grain	L	loam	fi	firm				
				Co	Coarse						
				G	gravelly						

The shift from alluvial to aeolian deposition at approximately 8670 ± 90 RCYBP (mid-soil) in the BCI profile and at 8200 ± 60 RCYBP (age-at- burial) at the Leavengood profile corresponds to regional patterns of increased aridity marked by aeolian deposition (9,10).

Radiocarbon ages were also cross-checked with cultural chronologies and biostratigraphy (1,11). The presence of an early Paleoindian age cache attributed to the Clovis culture (11) supports the pre-11,000 RCYBP age for the basal sands and gravels found below the lowest BCI T-5 soil radiocarbon dated to 10,985 ± 45 RCYBP (average of Beta-184854 11,070 ± 60 and Beta-262540 10,870 ± 70). A Clovis projectile point with elephant (e.g. mammoth) protein residue was recovered from sediments below the distinctive YD soil at the "Clovis" exposure

(11). Projectile points attributed to the Plainview culture were identified in deposits rendering soil dates averaging 10,685 ± 50 RCYBP (3) in the BCI terrace. This date for Plainview is consistent with the results of other researchers (12). The soil containing this cultural material is bracketed by soils dated to 10,407 ± 60 RCYBP (average of 10,400 ± 120, 10,410 ± 70) above and 10,985 ± 45 RCYBP below.

The paucity of early and middle Holocene cultural materials in the Bull Creek valley precludes a comparison of early and middle Holocene sediments to comparable cultural chronologies. Late Holocene cultural deposits are common on the surface and near-surface of the T-5 terraces along Bull Creek and adjacent drainages. Unfortunately, none of the radiocarbon dated late Holocene age soils contained cultural material. The only directly dated Late Holocene cultural material was a hearth in a T-2 terrace (Hearth locality). No soil organic carbon sample was dated to compare to the hearth charcoal radiocarbon date.

The late Pleistocene age for the lowest T-5 soil is further supported by the latest occurrence of mammoth remains in the Bull Creek valley (1). Mammoth was extirpated from the southern Plains at the end of the Pleistocene. Mammoth bones, tusks, teeth, and residue (see above) have been found in the deposits at the base of T-5 terraces within the Bull Creek drainage (11). The only large Rancho La Brean species to survive the late Pleistocene extinctions was *Bison antiquus* and it continues to be seen in Bull Creek deposits dating up to and including approximately 9000 RCYBP (13). The chronological distribution of taxa within Bull Creek is consistent with regional biostratigraphy (14,15).

Stable carbon isotope $\delta^{13}C$ curve developed from soil carbon samples associated with radiocarbon-dated soils along Bull Creek and within the Beaver River drainage (1) is compared with the Greenland ice core data(GISP 2 curve, 2) to provide a guide to the synchronicity of the project samples with paleo-temperature variations from ice cores (Figure S1.2). Fluvial terrace mapping, stratigraphic description, and grain-size analysis were employed to interpret the geomorphic evolution and depositional history of the Bull Creek valley.

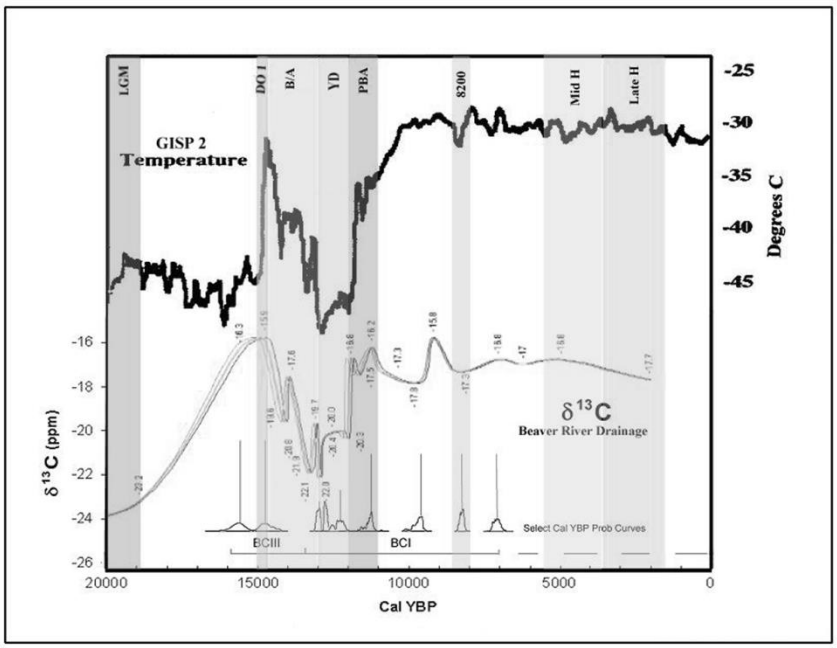

Figure S1.2. Comparison of stable carbon isotope trends. Stable carbon isotope $\delta^{13}C$ curve developed from soil carbon samples associated with radiocarbon-dated soils along Bull Creek and within the Beaver River drainage (16) compared with the Greenland ice core data (GISP 2 curve, 17) to provide a guide to the synchronicity of the project samples with paleo-temperature variations from ice cores.

1.2. Fluvial Terrace Mapping

The goal of mapping was to identify and outline the perimeter of each terrace tread present in the valley (Figure S1.3). Mapping was conducted using an RTK GPS system. The elevation data collected with our GPS system is accurate within 3 cm. The GPS receiver was attached to a backpack and set to record a point every 5 seconds. ArcGIS software was used to create a map of the Bull Creek terraces. GPS points and their elevations were initially plotted over an aerial photograph. Comparison of terrace outlines with respect to visible geomorphic features determined the lateral extent of each terrace tread. Exact elevations points were used to confirm terrace identification assigned in the field and correlate the discontinuous remnants of terraces across the valley. In some instances, identification adjustments were made. Five terraces, identified as T1, T2A, T2, T3 and T5, appear on the map. Some features, such as the creek channel, prominent gullies, and several alluvial fans, were also mapped using the aerial photographs. Finally, the features mapped for this study were superimposed over a geologic base map modified from Stanley et al. (18).

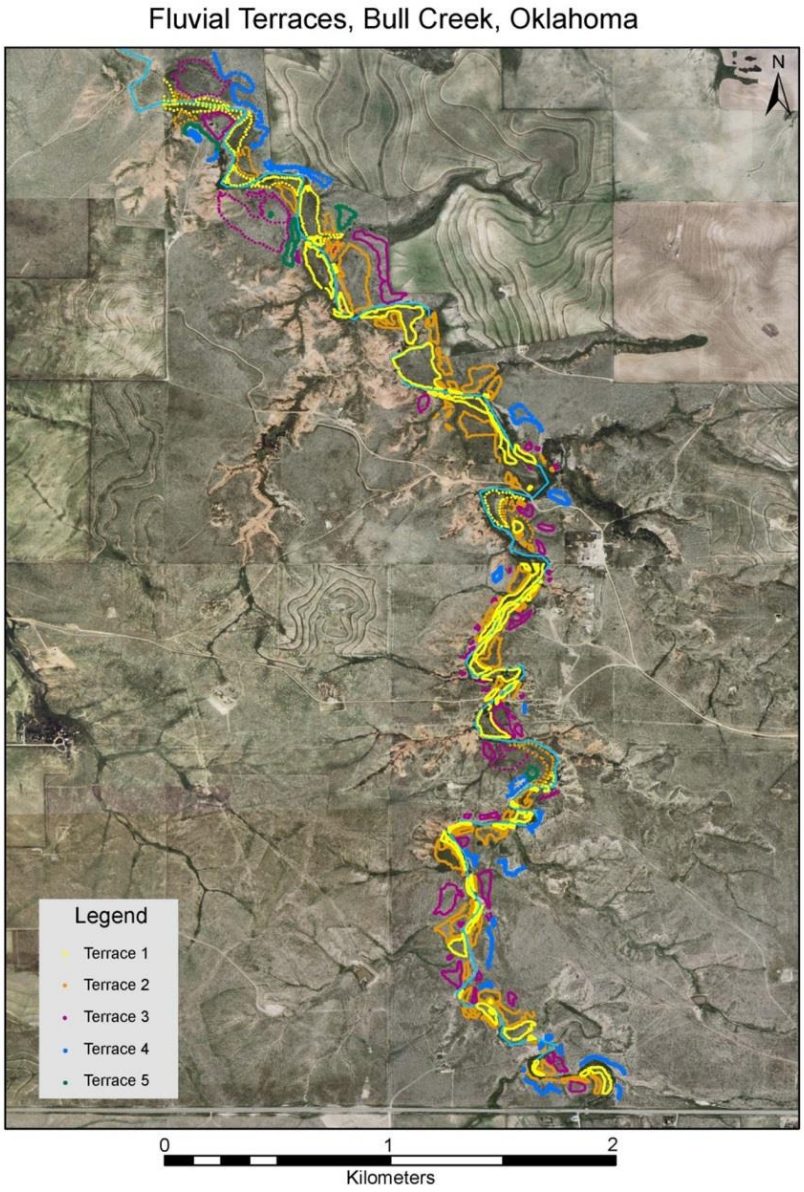

Figure S1.3. High precision mapping of Bull Creek terraces. Geo-stratigraphic and geophysical studies produced maps of the Bull Creek terraces (T0 through T5) were prepared to place the results within the Bull Creek setting. These products establish detailed contextual referents for the various sediment profiles.

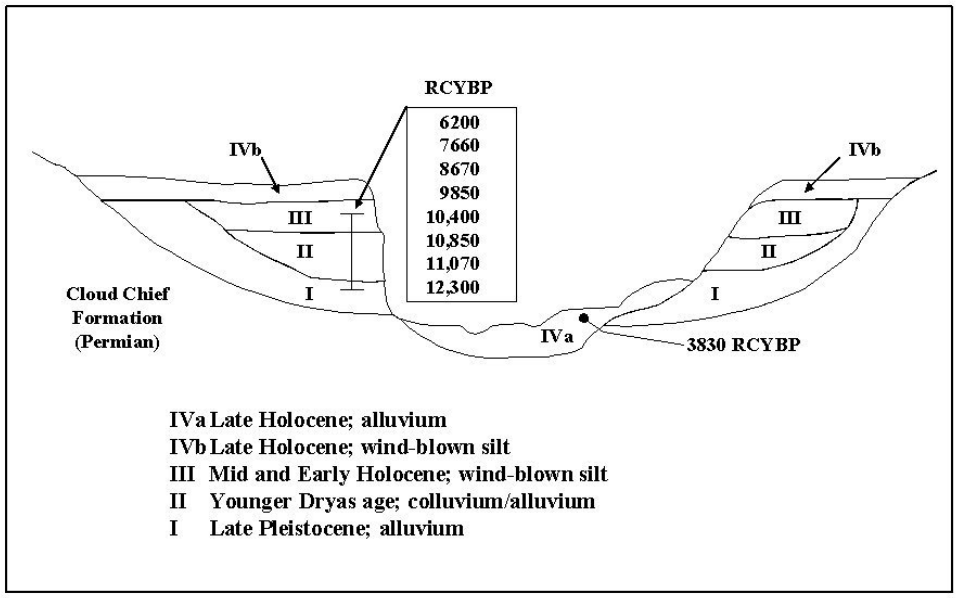

Figure S1.4. Schematic cross section of Bull Creek drainage showing T5 terrace sediments.

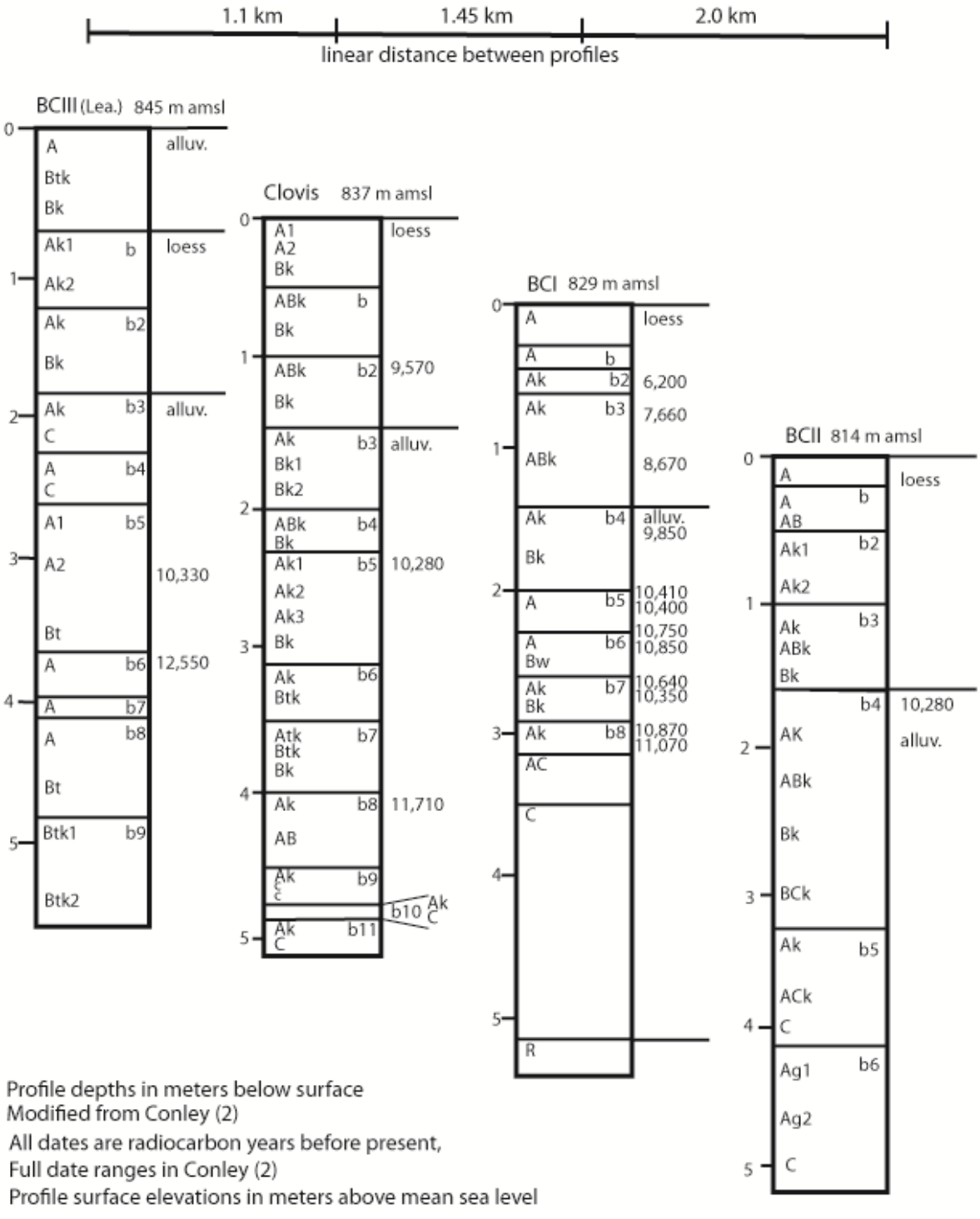

Figure S1.5. Vertical relationship of key Bull Creek profiles.

2. Sample processing for nanodiamond analyses

2.1. Methods

Nanodiamond extraction began on a series of test samples to verify the extraction protocols and to test the extraction equipment. The test extractions consisted of a pure nanodiamond sample obtained from commercial sources and nanodiamond-dosed sediment samples. The TEM analysis of these samples demonstrated successful application of extraction protocols and opened the door to begin the extraction and analysis of project samples. Upon completion of the test extraction, a total of 71 samples were processed for nanodiamond extraction. These samples target periods of known environmental perturbations (Figure S1.2) and sample depositional settings, including alluvial and aeolian events and pedologic events of various duration.

2.2. Soil Treatment of Concentrating Digestion-Resistant Particles

For each soil sample selected for acid digestion, particle-size analysis was determined by the hydrometer method (19,20,21) after passing through a 2 mm-sized sieve. Any soil material larger than 2 mm was weighed and recorded. One gram of clay (less than 2 microns, concentrated from particle-size analysis) was weighed exactly to the 4th decimal place (1 times 10 to the minus 4^{th}) and placed in a 250 ml polypropylene bottle. Each 1-gram clay sample received a 50 ml treatment of 30% H_2O_2; one 15 ml treatment of aqua regia; three separate treatments of 100 ml 48% HF (reacting over several days); three 100 ml treatments of saturated boric acid; and a 100 ml treatment of 0.1 N NH_4OH (additional treatments of 0.1 N NH_4OH as needed to reduce the concentration of HF to less than 3 ppm). Treatments applied above to remove extraneous soil material and concentrate nanodiamonds followed Jackson (22), Sridhar and Jackson (23), and Hossner (24; Method for Digestion with Aqua Regia and Hydrofluoric Acid in a Closed Vessel, pages 56 and 57). Decantation was employed to remove solution treatment waste. After the last decantation, the final solution (also containing digestion-resistant particles) mass remaining in the 250 ml bottle was recorded. All samples were treated and remained in the initial 250 ml polypropylene bottle until removed for TEM analysis.

2.3. Preparation of TEM grids

Nanodiamond samples were initially prepared by agitating the sample solutions in an ultrasonic bath for 5 minutes, and then depositing 10 μL of sample solution on a TEM grid and allowing it to air dry for ~1-3 minutes. Any remaining solution was then wicked away. No particles that could be confirmed as diamonds were observed on any of the grids prepared using this method.

A second TEM grid preparation method was developed to concentrate digestion-resistant particles, which would include nanodiamonds, from the sample solutions. The solutions were again agitated in an ultrasonic bath for 5 minutes, after which three milliliters of sample solution were deposited in a centrifuge tube. A TEM grid was placed in the tube and the tube was gently swirled until the TEM grid settled at the bottom of the tube. The sample was then centrifuged at 3000 rpm for 30 minutes. The TEM grid was then removed from the tube and any remaining solution was wicked away. Grids prepared using this second method contained significantly more particles than those prepared using the first method. Particle densities on some grids were too great to allow for accurate investigation. These samples were remounted using the same method, but were diluted with ultrapure water prior to centrifugation. Solution to water dilutions ranged from 1:1 to 1:3.

2.4. Recovery of cubic nanodiamonds in control experiments

Control experiments where ~5 nm cubic nanodiamonds purchased from a commercial vendor (Dynalene, www.dynalene.com, ND-90) were mixed with Bull Creek soil demonstrated recovery of added particles, including the entire expected diffraction pattern for cubic diamond (Table S3.1). These experiments showed that (1) our digestion procedure didn't destroy cubic nanodiamonds, (2) our methods led to the preservation of added diamonds, such that they were not lost during a washing / decanting step, and (3) we were able to verify our imaging and electron diffraction methods.

Table S3.1. Expected and measured interplanar spacings (in Å) of large putative hexagonal diamond grains. Observations from this study are in shaded columns.

cubic diamond	**observed commercial nano-diamond**	**hex-diamond**	**graphene**	**graphane**	**putative hex diamond**	**n-diamond Peng et al. (25)**	**observed nano-diamonds**
		2.18	2.13		2.12-2.18		
2.06	2.06	2.06		2.02	2.01-2.03	2.06	2.06
		1.92				1.78	1.78
		1.49					
1.26	1.27	1.26	1.23		1.23-1.24	1.26	1.26
		1.16		1.17	1.12-1.13		
1.08	1.09	1.09	1.06			1.07	1.06
0.89	0.91			1.01	1.03	0.90	
0.82	0.83		0.81			0.82	

3. Identification of nanodiamonds and carbonaceous grains

All sample digestion residues had both carbonaceous and non-carbonaceous components. The non-carbonaceous often amorphous groundmass contained major elements expected from a soil digestion. Additionally, iron oxide and abundant calcium fluoride was observed in several samples. Likely, the calcium fluoride precipitated after the HF treatment and was not from the original soil. EDS mapping revealed nanoparticulate titanium oxide and Pb-bearing particles as well.

3.1. Putative hexagonal diamonds: graphene-graphane

The basis for the mineralogical identification was electron diffraction. As the electron beam passes through a crystal, it is scattered in all directions (including forward, through the sample). The scattered electron waves destructively interfere, except at special angles directly related to the spacings between rows of atoms in the crystals. This phenomenon is diffraction. In an electron diffraction pattern, the distance between the central beam and the diffracted electron intensity can be converted to an interplanar spacing. The set of interplanar spacings, describing rows of atoms in various orientations, is compared with a list of interplanar spacings determined from X-ray diffraction measurements. Single nanocrystals are poorly suited to crystal structure solution by X-ray diffraction. In the TEM, phases such as graphene, graphane, and n-diamond that occur uniquely as <10 nm particles present a significant challenge for identification (Figure S3.1).

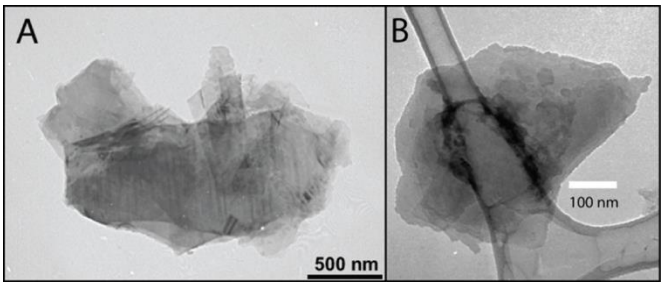

Figure S3.1. (A) Grain identified as hexagonal diamond by Kennett et al. (26), (B) example of analogous grains found in our samples.

Daulton et al. (27) demonstrated that using interplanar spacings from electron diffraction leads to ambiguities between nanodiamonds and other carbon phases such as graphene and graphane. One of the criticisms that Daulton et al. use to argue against the identification of the hexagonal nanodiamonds is that spots corresponding to the 1.92 and 1.49 Å (the (101) and (102) planes) are missing. Indeed, those spacings should be present in a randomly oriented polycrystalline aggregate of lonsdaleite (hex diamond) but are not seen in the Kennett et al. (26) work (Figure S3.2).

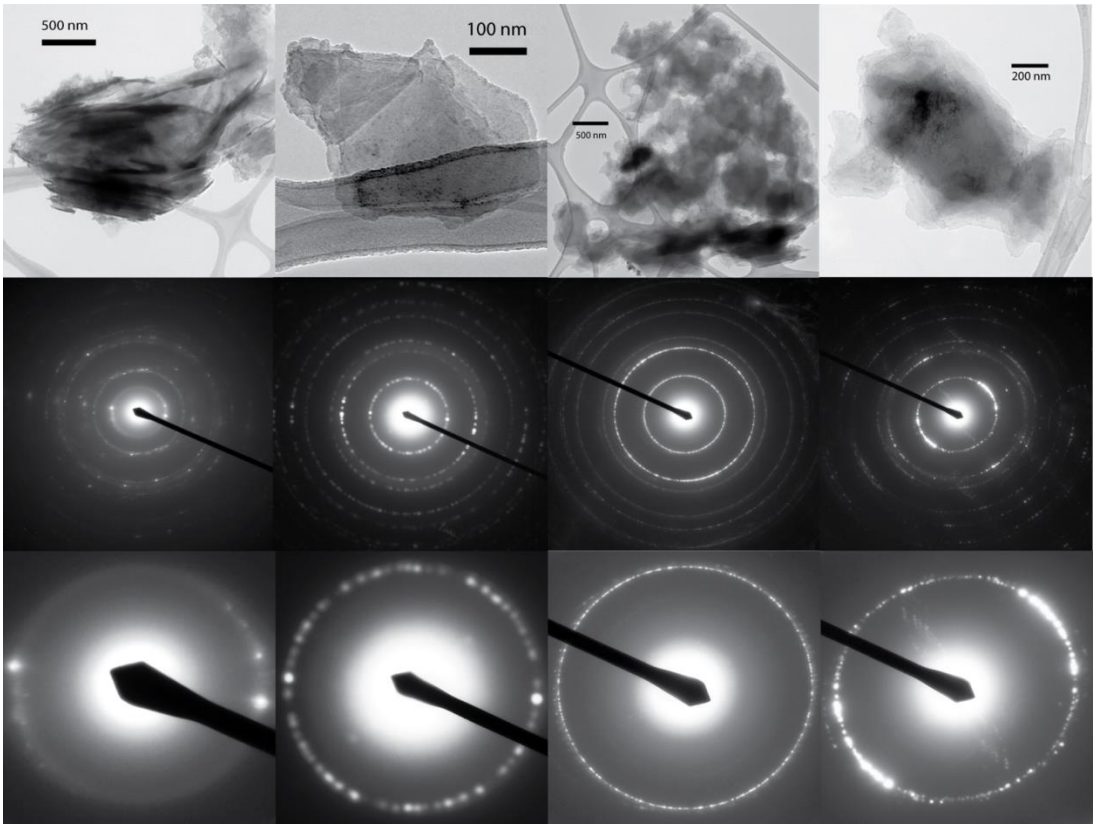

Figure S3.2. Examples of TEM images and corresponding electron diffraction patterns of putative hexagonal diamonds**.** Consistent with cubic diamond, graphene, graphane, graphite, or their mixtures. Diffraction patterns for each grain are located directly below. The bottom row includes a zoomed-in view of the rings corresponding to ~2 Å. The third grain is an example of the split suggested in Daulton et al. (27) to represent a graphene/graphane mixture.

Our electron diffraction patterns typically appear similar to those presented by Daulton et al. (27), although with variation. While this is not entirely conclusive (for example, the reflection spots could potentially be too weak to observe, although we do not deem this likely), it suggests that grains in our samples match graphene/graphane more closely than diamond. Given the interplanar spacings for graphane listed in Table S3.1, we are inclined to agree that this is a stronger match since we also do not observe the expected 2.18, 1.92, or 1.49 Å spacings for hexagonal diamond. Another possible interpretation is a mixture of cubic diamond and graphane (Table S3.1). In this case, we are missing the 0.89 Å spacing that we *do* observe in the commercial diamonds. Figure S3.3 illustrates the close correspondence is between the electron diffraction patterns from some of our samples with those identified by Daulton et al. as graphene and graphane.

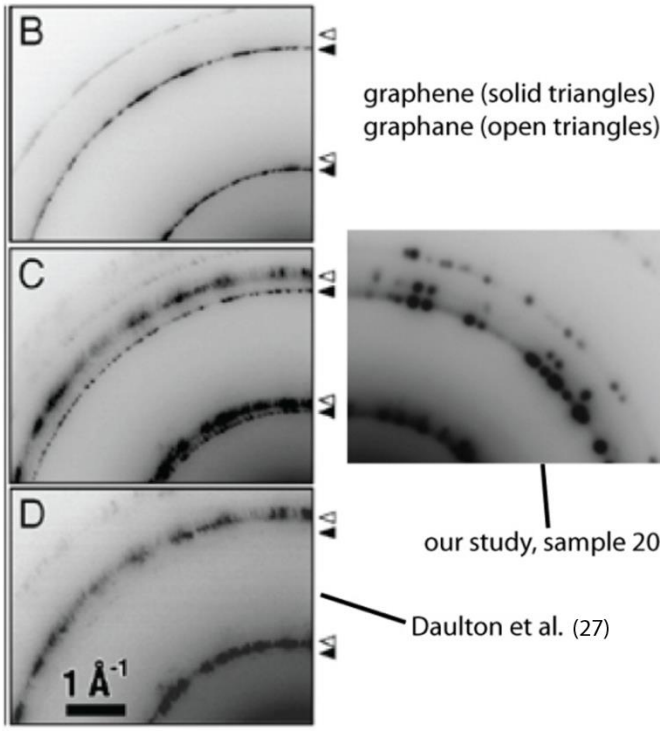

Figure S3.3. Comparison of electron diffractions from Daulton et al. (27) with putative hexagonal diamonds. Left column: electron diffraction patterns for polycrystalline graphene (solid triangles, top), graphane (open triangles, bottom), and mixtures of graphene/ graphane (middle) as given in Daulton et al. (27). Right: one of our electron diffraction patterns from sample BC20 presented at a similar scale. Note the similarity to the graphene/graphane mixture.

3.2. On the identification of n-diamonds

Lattice fringes and selected-area electron diffraction patterns of typical observed nanodiamonds resulted in spacings coincident with n-diamond as in Peng et al. (25) (Table S3.1, Fig. S3.4, S3.5). The grain sizes and morphologies were generally consistent, with a few exceptions. Sintering, where oblong nanodiamond particles formed by joining multiple sub-grains, was observed commonly only in two of the samples (LEA 22 and BC 34). BC36 had few grains, but much larger grain sizes than those observed in other samples.

There is some doubt in the scientific community as to the nature of n-diamond and its validity as a true diamond phase. Hirai and Kondo (28) first used the term "n-diamond" to indicate a "new" phase observed in quenched experiments with shocked graphite. The designation as a new phase was based primarily on the observations of diffracted intensity from interplanar spacings that are forbidden by symmetry in cubic diamond. For example, diffracted intensity from the {200} planes of cubic diamond are not observed because the scattering from the {100} planes are exactly out of phase with scattering from the {200} planes, leading to complete destructive interference. The observation of diffracted intensity at the ~1.8 Å interplanar spacing expected for the {200} plane is thus diagnostic for the n-type diamond polymorph and indicates some change in the structure that leads the {100} and {200} planes to no longer be equivalent, in terms of their electron and X-ray scattering power.

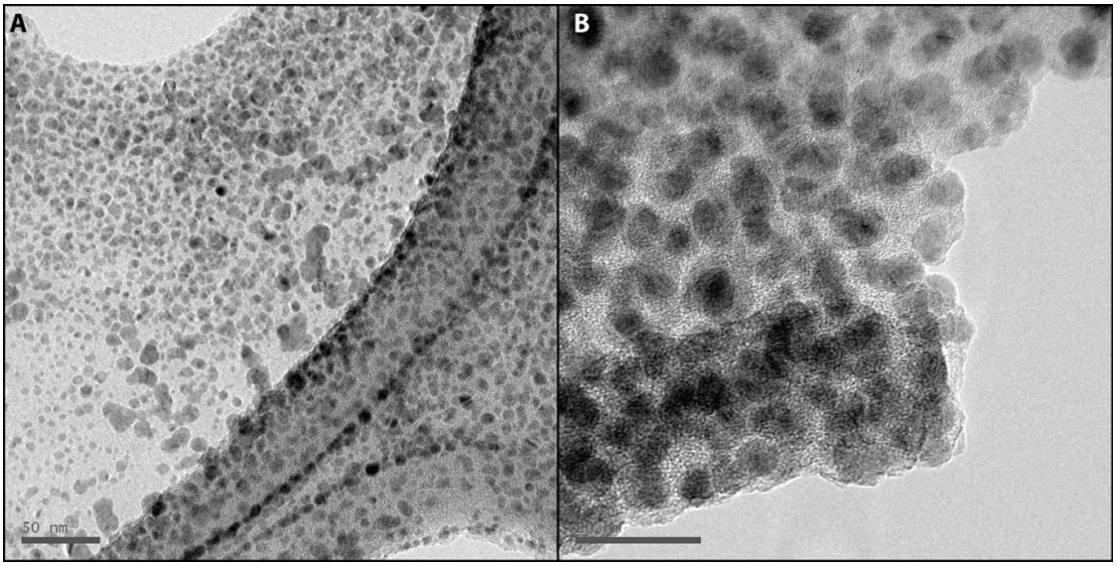

Figure S3.4. TEM images of typical nanodiamonds, in this case from BC51. Scale bars are (A) 50 nm and (B) 20 nm.

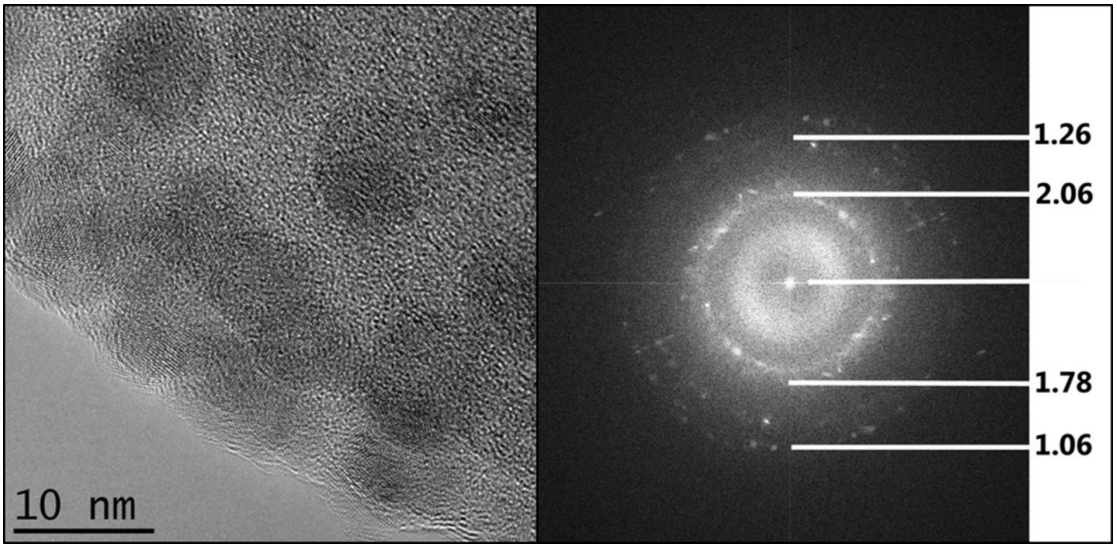

Figure S3.5. TEM and SAED pattern of typical nanodiamonds.

Several attempts have been made to propose n-diamond structures (e.g., 29,30,31). Several of the proposed structures appear inconsistent with existing models of carbon bonding. Others have suggested that observed "forbidden" reflections result from dynamical diffraction processes, where the electron waves scatter off of multiple {111} twin boundaries (e.g., 32,33) or small-particle effects between multiple nanoparticles (34). In fact, the specific example of diamond {200} forbidden reflections appearing in TEM analyses was given in a high-resolution TEM textbook (35). However, the {200} reflection was also observed in X-ray diffraction studies, in which X-rays are much less susceptible to dynamical diffraction effects (e.g., 31).

Perhaps most convincingly, electron nanobeam diffraction patterns of single n-diamond nanocrystals were shown to be consistent with a structure intermediate between cubic diamond and FCC carbon and considered by one of the leading TEM experts (e.g., 36,37) to be a real phase (38). In their model, the diffracted intensities could be reproduced if hydrogen replaces a variable amount of C on existing atomic sites. This model was recently supported by ab-initio computational modeling and powder X-ray diffraction (39).

The 'forbidden' reflections used to distinguish n-diamond have actually been observed quite commonly in nanodiamonds formed in a variety of processes and environments, including natural sediments (e.g., 26,40,41,42), low-pressure chemical vapor deposition (e.g., 43,44) laser bombardment of amorphous carbon films (45), natural uranium-rich rocks associated with radioactive decay (32), high pressure treatment of graphite (46), "detonation" nanodiamonds resulting from exploding carbon powders (e.g., 47), shock-compressed C_{60} films (48), and Mexican crude oils (49). Ishimaru et al. (50) report one occurrence consistent with n-diamond from residue of wood charred to 700°C for 1 hour. However, their material was unstable in the electron beam, unlike the n-diamonds in this study.

Electron Energy Loss Spectroscopy (EELS) provides another line of evidence toward identification of the n-diamonds. The carbon core energy loss spectra change depending on the details of the bond geometries and nearest neighbors surrounding all of the atoms in the analysis area (e.g., 51,52). In a simplified sense, features corresponding to "π" or sp^2-type bonding and "σ" or sp^3-type bonding can be distinguished. It should be remembered that in most instances, grains of interest rest on amorphous carbon-type carbon film dominated by sp^2 carbon. Like Daulton et al. (27), EELS spectra of large flake-like particles (e.g., Figure S3.2.) were consistent with sp^2 bonding and graphene/ graphane.

EELS of grains identified by SAED and HRTEM as n-diamond (Figure S3.6.) were consistent with literature spectra. A grain identified by Kurbatov et al. (40) by HRTEM as n-diamond matches our spectra (Figure S3.6A-B). Studies such as Daulton et al. (27) and Stroud et al. (53) clearly illustrate additional features in EELS of cubic nanodiamonds (e.g., Figure S3.6C). Studies of diamond formation by carbon ion implantation in quartz show a transition in EELS coincident with the production of either cubic or n-diamonds. Specifically, the spectra transitioned from spectra similar to the top line of Figure S3.6C with additional features attributed to σ-type bonds to spectra matching those of Figure S3.6A and S3.6B (54,25). Thus, while the spectra were consistent with other work on n-diamond, they were not particularly useful for discriminating between n-diamond and sp^2-dominated phases such as graphene and graphite.

3.3. On the identification of cubic NDs.

Cubic nanodiamonds were not unequivocally identified in our sediments, except in control samples where commercial cubic NDs were added. SAED patterns were not sufficient to distinguish cubic diamond from other carbon forms (e.g., 27). In some samples, HRTEM images revealed particle sizes and lattice fringes consistent with cubic diamond. An example is shown in Figure S3.7. HRTEM imaging of commercial cubic

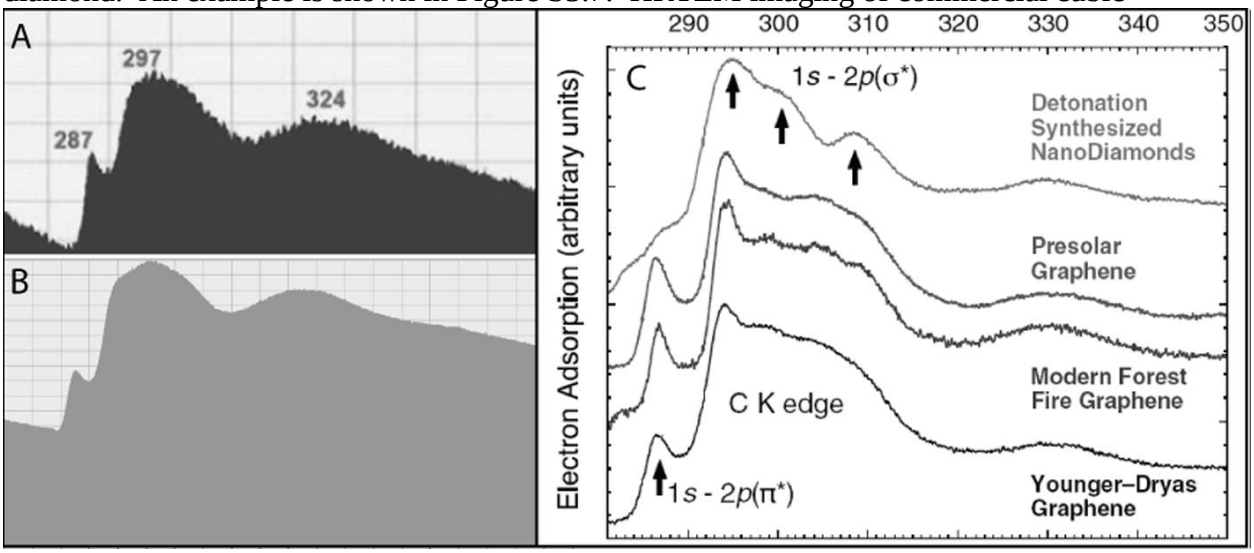

Figure S3.6. EELS spectra. **(**A) Reported EELS spectra for n-diamond from Kurbatov et al. (40), (B) the analysis spot on an n-diamond on top of a flake-like particle from this study, and (C) EELS from various relevant materials reported by Daulton et al. (27), except for n-diamond.

diamonds reveals a distribution of fringes consistent with diamond {111} (Figure S3.7., top). However, a similar distribution of fringes can be obtained from amorphous areas (Figure S3.7., bottom), such that neither fringes nor SAED can be used for positive identification of cubic nanodiamonds. As mentioned earlier, it may be possible that diamonds identified in our work as n-diamonds are actually cubic NDs exhibiting kinematic diffraction effects that lead to the presence of the normally forbidden {200} spacing due to their somewhat larger size, defects, and/or twinning.

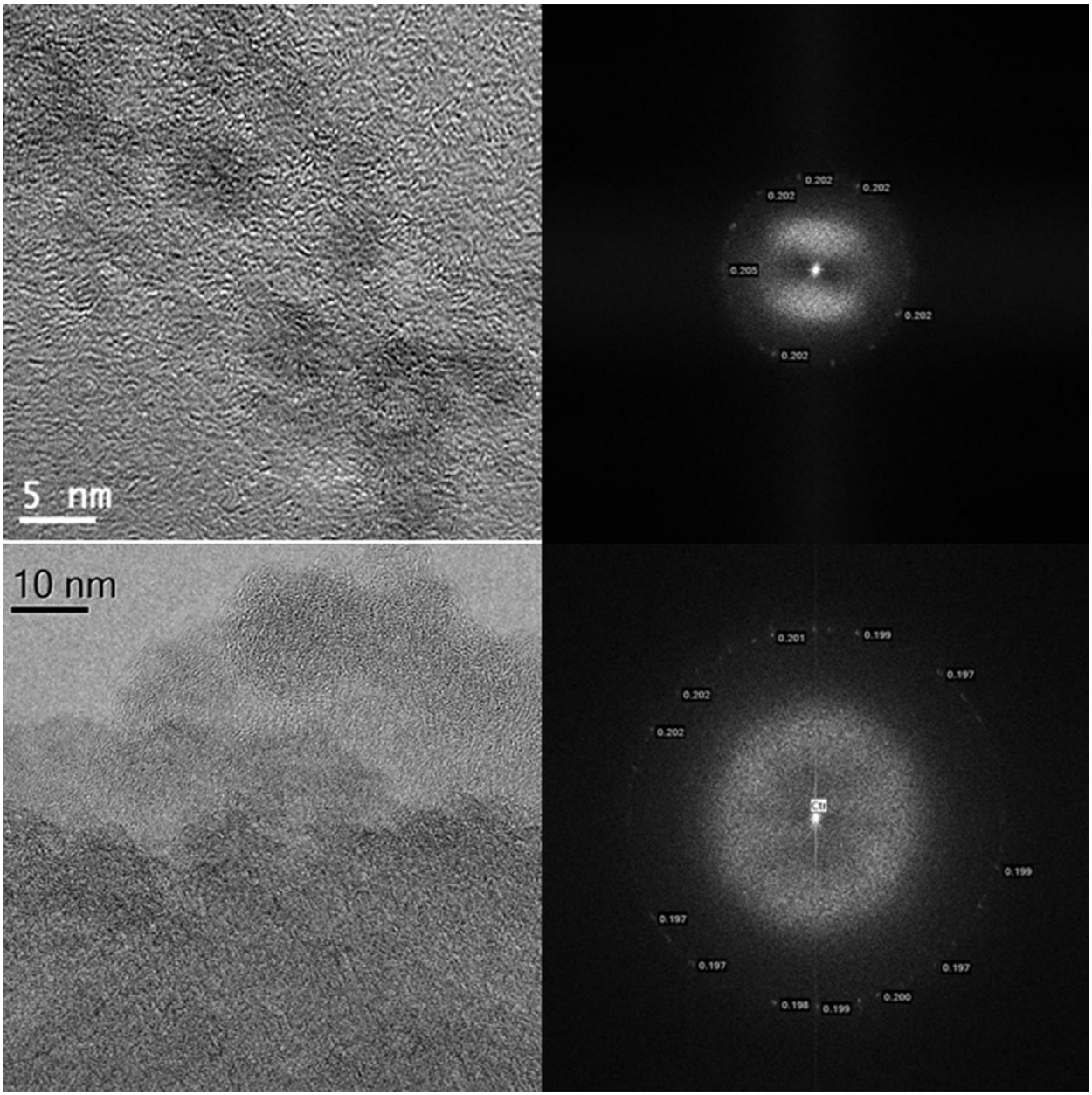

Figure S3.7. TEM images and Fast-Fourier Transforms (FFTs) of commercial cubic nanodiamonds compared to soil digest.

4. Quantification of Nanodiamonds

Sediment digestion residues that were observed to have nanodiamonds were qualitatively ranked on an arbitrary scale from 1-3, with 1 referring to samples with few nanodiamonds, and 3 referring to samples with abundant nanodiamonds. They were independently ranked by Swindle based on observations in conventional TEM and Madden based on observations with HRTEM. No sample differed in qualitative rank by more than one level; most samples found agreement. In cases of disagreement, the value determined by conventional TEM was chosen due to the

much greater area of each grid used to make observations. Some samples were assigned values that straddled the boundary between categories.

One sample from each qualitative rank was chosen for quantification. The nanodiamond quantification procedures used in this investigation were modified from Kennett et al. (26). The first step of the modified procedure was to determine the concentration of non acid-digestible solids in each of the sample solutions. This was done by weighing empty centrifuge tubes, filling them with 9 ml of solution, weighing the full tubes, and centrifuging the tubes at 15,000 rpm for 1 hour. After which, the supernatant was poured off, and the tubes were allowed to air dry before being reweighed. Once the concentration of non acid-digestible solids in 9 ml of sample was determined, total non acid-digestible concentrations (C_{init}) were calculated for the three samples selected for quantification. Nanodiamond counts were then made for each of the three samples using TEM. For each sample, 21 grid windows were examined for the presence of nanodiamonds. For windows containing nanodiamonds, the percentage coverage of nanodiamonds was estimated as was the ratio of nanodiamonds to amorphous/non-diamond material. Arithmetic means for nanodiamond percent coverage (ND_{cov}) and nanodiamond to other material ratios (ND_{ratio}) were calculated for each sample, as was a percentage of TEM grid windows containing nanodiamonds (W_{ND}). Final nanodiamond concentrations were calculated using the equation:

$$ND(ppm) = C_{init} * W_{ND} * ND_{cov} * ND_{ratio}$$

Calculated concentrations corresponding to qualitative ranks of 1, 2, and 3, were 0.5, 1.9, and 190 ppm, respectively. Samples with a qualitative rank represent 'spikes' in the nanodiamond distribution, outpacing even a logarithmic relationship between qualitative and quantitative measurements (Figure S4.1).

Next, the concentrations (ppm) determined by quantification were applied to the broader suite of samples. Samples assigned intermediate qualitative values (i.e., 1-2) were assigned ppm

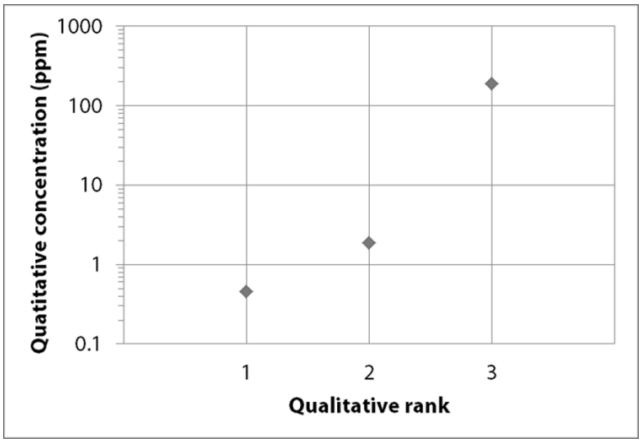

Figure S4.1. Comparison of qualitative ranking with quantitative concentration. Quantitative axis is logarithmic.

concentrations intermediate between the two categories. The 'Bull Creek' profile, corresponding to the same working face as that studied by Kennett et al. (26), represents a continuous series of extracted samples from BC19 (oldest) to BC52 (youngest). The distribution of nanodiamonds is

described by spikes at BC20 and BC51-52, with much smaller concentrations observed in C23-25 and BC34-36 and BC 38 (Figure S4.2).

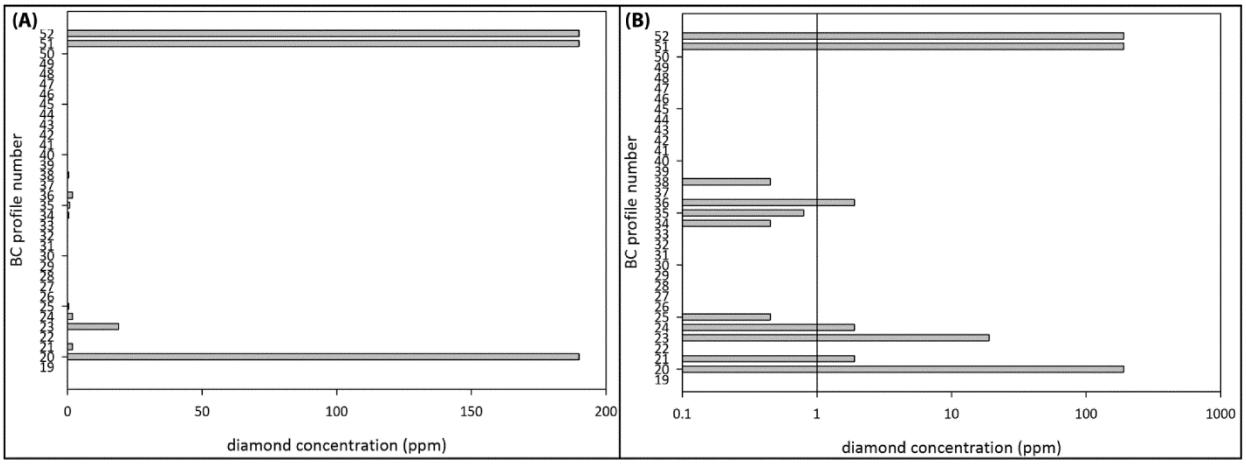

Figure S4.2. BC profile nanodiamond distribution with (A) linear and (B) log scales.

Additional samples were analyzed in other profiles in the Bull Creek area. No nanodiamonds were found in "Blue Mound" samples. Out of six "Hearth" samples, nanodiamonds with qualitative rank of '1' were found in three. Diamonds were much more abundant in the "Leavengood" samples, as suggested by the data in Table 1.

5. Calculations of surface exposure ages.

Time of surface exposure of containing units was estimated to determine if ND presence is simply a result of cosmic NDs settling on Earth's surface and accumulating over time. This test was only applied to Bull Creek I. In this case radiocarbon ages obtained from soil organic matter are assumed to represent soil burial ages. The time a soil was present at the surface was estimated by subtracting its age from the age of the soil below it. In theory, the longer a soil is present at the surface, the more abundant NDs within it should be. However no correlation was found between ND abundance and surface exposure time (Figure S5.1).

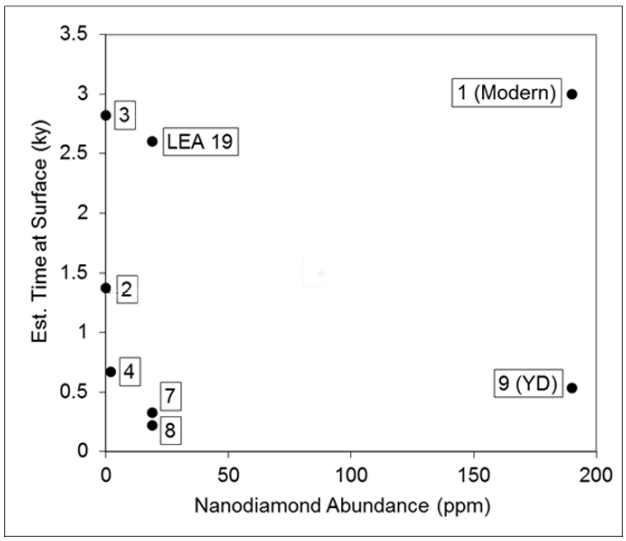

Figure S5.1. Nanodiamond abundance versus estimated exposure time of the sample exposed at the depositional surface. Sample labels correspond to sample numbers in Table 1. 1(BC1 52& 51), 2 (BC1 46), 3 (BC1 43), 4 (BC1 36), 5 (BC1 30), 6 (BC1 28), 7 (BC1 26), 8 (BC1 21), 9 (BC1 20), and LEA 19 (LEA 19). "YD" corresponds to the Younger Dryas boundary.

6. Relation to cultural artifacts

The vertical distribution of cultural artifacts (burned and unburned) are plotted against nanodiamond frequency for the BCI samples (Figure S6.1).

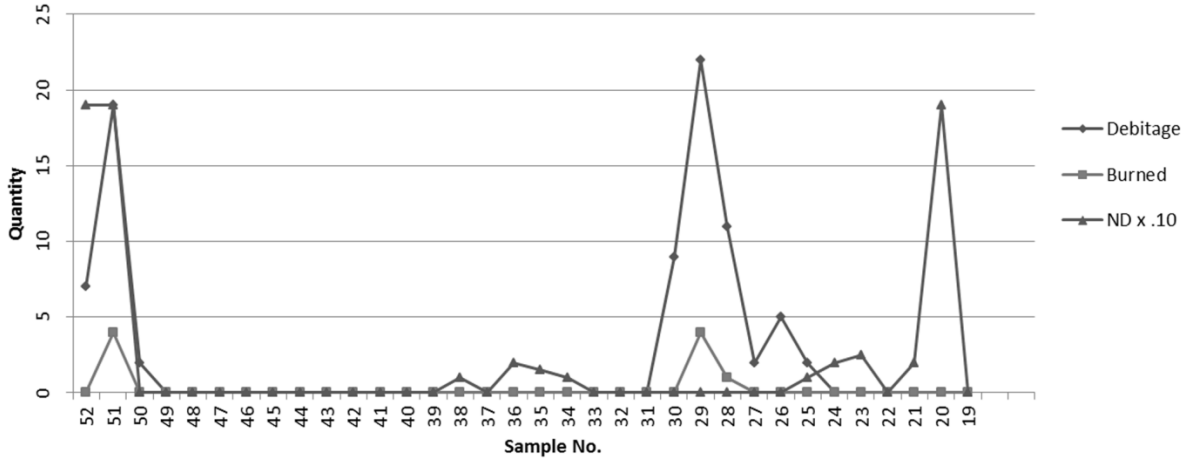

Figure S6.1. Comparison of lithic cultural material quantity with nanodiamond occurrence at BC1.

7. References

1. Bement LC, Carter BJ, Varney RA, Cummings LS, Sudbury JB (2007a) Paleo-Environmental Reconstruction and Bio-Stratigraphy, Oklahoma Panhandle, USA. *Quat Internat* 169-170: 29-50.
2. Conley TO (2010) Buried Soils of Late Pleistocene to Holocene Ages Accented in Stacked Soil Sequences from the Southern High Plains of the Oklahoma Panhandle. Unpublished MS Thesis, Department of Soil and Plant Sciences, Oklahoma State University, Stillwater.
3. Bement LC, Carter BJ (2010a) An Early Occurrence of Plainview in the Oklahoma Panhandle. *Curr Res Pleist* 27:67-69.
4. Goslar T et al., (1995) High concentration of atmosphere ^{14}C during the Younger Dryas. *Nature* 377:414‑417.
5. Carter, BJ, Bement LC (2004) Late Quaternary Soil-Sediment Stratigraphy and Cultural Materials along Bull Creek, Oklahoma Panhandle. *Curr Res Pleist* 21:119-122.
6. Conley TO, Carter BJ, Bement LC (2009) Late-Pleistocene/Early-Holocene Boundary, Buried Soils, Loess, and Alluvium throughout the Bull Creek Drainage, Oklahoma Panhandle. *Curr Res Pleist* 26:193-195.
7. Haynes CV, Jr. (2008) Younger Dryas "black mats" and the Rancholabrean termination in North America. *Proc Natl Acad Sci USA* 105(18):6520-6525.
8. Reimer PJ, et al. (2009) IntCal09 and Marine09 radiocarbon age calibration curves, 0–50,000 years cal BP. *Radiocarbon* 51(4):1111–50.
9. Holliday VT, Meltzer DJ, Mandel R (2011) Stratigraphy of the Younger Dryas Chronozone and Paleoenvironmental Implications: Central and Southern Great Plains. *Quat Internat* 242:520-533.
10. Mandel RD (2008) Buried Paleoindian-age Landscapes in Stream Valleys of the Central Plains, USA. *Geomorph* 101:342-361.
11. Bement L, Schuster K, Carter B (2007b) Archeological Survey for Paleo-Indian Sites along the Beaver River, Beaver County, Oklahoma. Oklahoma Archeological Survey *Archeological Resource Survey Report No. 54*. University of Oklahoma.
12. Holliday VT, Johnson E, Stafford TW, Jr. (1999) AMS Radiocarbon Dating of the Type Plainview and Firstview (Paleoindian) Assemblages: The Agony and the Ecstasy. *Am Antiq* 64:444-454.
13. Bement L, Buehler K, Carter B (2012) Ravenscroft: A Late Paleoindian Bison Kill in the Oklahoma Panhandle. *Oklahoma Anthropol Soc Bull* 60:17-30.
14. Dalquest WW, Baskin JA (1992) Mammals of the Elm Creek Local Fauna, Late Pleistocene of Beaver County, Oklahoma. *Amer Midland Naturalist* 127:13-20.
15. Johnson E (1987) Vertebrate Remains. In: Johnson, E. (Ed.), Lubbock Lake: Late Quaternary Studies on the Southern High Plains. Texas A&M University Press, College Station, pp. 49-89.
16. Bement LC, Carter BJ (2008). A Younger Dryas Signature on the Southern Plains. *Curr Res Pleist* 25:193-194.
17. Alley RB (2000). The Younger Dryas Cold Interval as Viewed from Central Greenland. *Quat Sci Rev* 19:213-226.
18. Stanley TM, Suneson N H, Standridge GR (2002) Geologic Map of the Beaver 60' X 30' Quadrangle, Beaver, Ellis, Harper, and Texas Counties, Oklahoma. Oklahoma Geologic Quadrangle OGQ-37.

19. Gee GW, Bauder JW (1986) Particle-size analysis. In: Methods of Soil Analysis, Part 1, Physical and Mineralogical Methods. Agronomy Monograph no. 9, second ed. Soil Science Society of America, Madison, WI.
20. Alexander HM (2013) The Stratigraphic and Geomorphic Evolution of the Bull Creek Valley, Oklahoma: Implications for Paleoclimate Studies and Nanodiamond Occurrence. MS Thesis, University of California, Santa Barbara, Santa Barbara, CA. 93 pp.
21. Gee GW, Orr D (2002) Particle-size analysis. *In* Methods of Soils Analysis. Part 4. J. H. Dane and G. C. Topp (eds.). Soil Science Society of America Book Series No. 5. Soil Science Society of America Inc., Madison, WI, pp. 255-293.
22. Jackson ML (1979) Soil Chemical Analysis – Advanced Course. 2nd Edition, 11th printing. Published by the author, Madison, WI.
23. Sridhar K, Jackson ML (1974) Layer charge decrease by tetrahedral cation removal and silicon incorporation during natural weathering of phlogopite to sponite. *Proc Soil Sci Soc Amer* 38:847-850.
24. Hossner LR (1996) Dissolution of Total Elemental Analysis. *In* Methods of Soils Analysis. Part 5. D. L. Sparks (ed). Soil Science Society of America Book Series No. 5. Soil Science Society of America Inc., Madison, WI, pp. 49-64.
25. Peng JL, Bursill LA, Jiang B, Orwa JO, Prawer S (2001) Growth of c-diamond, n-diamond and i-carbon nanophases in carbon-ion implanted fused quartz. *Philosophical Magazine B*, 81(12), 2071-2087.
26. Kennett DJ, Kennett JP, West A, Mercer C, Que Hee SS, Bement L, Bunch TE, Sellers M, Wolbach WS (2009) Nanodiamonds in the Younger Dryas boundary sediment layer. *Science* 323, 94-95.
27. Daulton TL, Pinter N, Scott AC (2010) No evidence of nanodiamonds in Younger–Dryas sediments to support an impact event. *Proc Natl Acad Sci USA* 107 (37), 16043–16047.
28. Hirai H, Kondo K (1991) Phases of Diamond Formed Under Shock Compression and Rapid Quenching. *Science* 253, 772-774.
29. Hirai H, Kondo K, Sugiura H (1992) Possible structural models of *n*-diamond: a modified form of diamond. *Appl Phys Lett* 61(4), 414-416.
30. Wen B, Zhao JJ, Li T, Dong C, Jin J (2006) Time-evolutional X-ray diffraction of n-diamond: An intermediate state between fcc and diamond structure. *Diamond & Related Materials*, 15, 1323-1328.
31. Wen B, Zhao JJ, Li TJ (2007) Synthesis and crystal structure of n-diamond. *Internat Mater Rev*, 52(3), 131-151.
32. Amaratunga G, Putnis A, Clay K and Milne W (1989) Crystalline diamond growth in thin films deposited from a CH4/Ar rf plasma. *Appl Phys Lett* 55, 634–635.
33. Daulton TL, Ozima M (1996) Radiation-Induced Diamond Formation in Uranium-Rich Carbonaceous Materials. *Science* 271, 1260–1263.
34. Tian H, Schryvers D, and Claeys P (2011) Nanodiamonds do not provide unique evidence for a Younger Dryas impact. *Proc Natl Acad Sci USA* 108(1), 40-44.
35. Spence JCH (2003) *High-Resolution Electron Microscopy*, Oxford University Press.
36. Cowley JM (1993) *Electron diffraction techniques. 2 (1993)*, Oxford University Press.
37. Buseck P, Cowley J, Eyring L. eds. (1989) *High-Resolution Transmission Electron Microscopy: and Associated Techniques*., Oxford University Press, USA.
38. Cowley JM, Mani RC, Sunkara MK, O'Keefe M, Bonneau C (2004) Structures of carbon nanocrystals. *Chem Mater* 16, 4905-4911.

39. Wen B, Melnik R, Yao S, Li T (2011) Hydrogen-doped cubic diamond and the crystal structure of n-diamond. *Chem Phys Lett* 516, 230-232.
40. Kurbatov AV, et al. (2010) Discovery of a nanodiamond-rich layer in the Greenland ice sheet. *J Glaci* 56(199), 747-757.
41. Israde-Alcántara I., et al. (2012) Evidence from central Mexico supporting the Younger Dryas extraterrestrial impact hypothesis. *Proc Natl Acad Sci USA* **109**, E738–E747.
42. Hoesel A. van, et al. (2012b) Nanodiamonds and wildfire evidence in the Usselo horizon postdate the Allerød-Younger Dryas boundary. *Proc Natl Acad Sci USA* **109**, 7648–7653.
43. Frenklach M, et al. (1989) Homogenous nucleation of diamond powder in the gas phase. *J Appl Phys* 66(1):395-399.
44. Buerki PR and Leutwyler S (1991) Homogenous nucleation of diamond powder by CO_2-laser-driven gas-phase reactions. *J Appl Phys* 69(6):3739-3743.
45. Hashavardhan KS, Yalamanchi RS, Rao LK (1989) Formation of crystalline diamond from amorphous diamond-like carbon films by pulsed laser irradiation. *Appl Phys Lett* 55(4), 351-353.
46. Endo S, Idani N, Oshima R, Takano KJ, Wakatsuki M (1994) X-ray diffraction and transmission-electron microscopy of natural polycrystalline graphite recovered from high pressure. *Physical Review B* 49(1), 22-27.
47. Terranova ML, et al. (2009) Self-assembly of n-diamond nanocrystals into supercrystals. *Crystal Growth & Design* 9(3), 1245-1249.
48. Yamada K and Sawaoka AB (1994) Very small spherical crystals of distorted diamond found in a detonation product of explosive/ graphite mixtures and their formation mechanism. *Carbon* 32(4), 665-673.
49. Santiago P, Camacho-Bragado GA, Marin-Almazo M, Murgich J, José-Yacaman M (2004) Diamond polytypes in Mexican crude oil. *Energy & Fuels* 18, 390-395.
50. Ishimaru K, et al. (2001) Diamond and pore structure observed in wood charcoal. *Journal of Wood Science* 47, 414-416.
51. Egerton RF (1996) *Electron Energy-Loss Spectroscopy in the Electron Microscope* (2nd ed.; New York: Plenum).
52. Stöckli, T (2003) Electron energy-loss spectroscopy of carbon nanotubes and onions. In *Electron Microscopy of Nanotubes*, Wang ZL and Hui C (eds.), Kluwer Academic Publishers.
53. Stroud RM, Chisholm MF, Heck PR, Alexander CMO'D, Nittler LR (2011) Supernova shock-wave-induced co-formation of glassy carbon and nanodiamond. *Astrophysical Journal Letters*, 738:L27.
54. Orwa JO, et al. (2001) Diamond nanocrystals formed by direct implantation of fused silica with carbon. *J Appl Phys* 90(6), 3007-3018.